

Topological phase transition of deformed \mathbb{Z}_3 toric code

Yun-Tak Oh¹, Hyun-Yong Lee^{1, 2*}

¹ Division of Display and Semiconductor Physics, Korea University, Sejong 30019, Korea

² Department of Applied Physics, Graduate School, Korea University, Sejong 30019, Korea

* hyunyong@korea.ac.kr

Abstract

We investigate the topological phase transitions of the deformed \mathbb{Z}_3 toric code, constructed by applying local deformations to the \mathbb{Z}_3 cluster state followed by projective measurements. Using the loop-gas and net configuration framework, we map the wavefunction norm to classical partition functions: the $Q = 3$ Potts model for single-parameter deformations and a novel \mathbb{Z}_3 generalization of the Ashkin-Teller model (AT_3) for the general two-parameter case. The phase diagram, obtained via the projected entangled pair state (PEPS) representation and the variational uniform matrix product state (VUMPS) method, exhibits three phases—the toric code phase, an e -confined phase, and an e -condensed phase—separated by critical lines with central charges $c = 4/5$ (\mathbb{Z}_3 parafermion conformal field theory) and $c = 8/5$, along with isolated antiferromagnetic critical points at $c = 1$ (\mathbb{Z}_4 parafermion conformal field theory). At these critical points, the system reduces to a square ice model with an emergent $U(1)$ 1-form symmetry, exhibiting Hilbert space fragmentation and quantum many-body scar states. Unlike the \mathbb{Z}_2 case, the absence of a sign-change duality leads to a richer phase structure.

Copyright attribution to authors.

This work is a submission to SciPost Physics.

License information to appear upon publication.

Publication information to appear upon publication.

Received Date

Accepted Date

Published Date

Contents

| | | |
|----------|---|-----------|
| 1 | Introduction | 2 |
| 2 | Models | 3 |
| 2.1 | \mathbb{Z}_N Toric Code | 3 |
| 2.2 | Cluster State: Toric Code Ground State | 4 |
| 3 | Generating Deformed \mathbb{Z}_3 Toric Code | 6 |
| 3.1 | Deformed \mathbb{Z}_3 Cluster State | 6 |
| 3.2 | Deformed Toric Code State and Parent Hamiltonian | 8 |
| 4 | Phase Diagram of Deformed \mathbb{Z}_3 Toric Code | 10 |
| 4.1 | Phase Diagram of $ \tilde{\Psi}(\beta_z)\rangle$ | 10 |
| 4.1.1 | Loop and Net Description | 10 |
| 4.1.2 | Mapping to Classical Potts Model | 12 |
| 4.1.3 | Emergent $U(1)$ 1-Form Symmetry and Hilbert Space Fragmentation | 13 |
| 4.2 | Phase Diagram of $ \tilde{\Psi}(\beta_x)\rangle$ | 14 |

| | | |
|----------|--|-----------|
| 4.2.1 | Loop and Net Description | 14 |
| 4.2.2 | Mapping to Classical Potts Model | 15 |
| 4.2.3 | Square Ice in Dual System | 16 |
| 5 | Tensor Network Analysis | 18 |
| 5.1 | Generalized Deformed \mathbb{Z}_3 TC | 18 |
| 5.2 | Mapping to Classical Ashkin-Teller Like Model | 19 |
| 5.3 | PEPS Representation and Injective Symmetries | 21 |
| 5.4 | Phase diagram | 24 |
| 5.5 | Criticalities | 25 |
| 6 | Conclusion | 25 |
| A | Review: Deformed \mathbb{Z}_2 Toric Code | 27 |
| A.1 | Loop-gas picture | 27 |
| A.2 | Wavefunction deformation | 28 |
| A.3 | Mapping to classical Ising model | 28 |
| A.4 | Mapping to Ashkin-Teller model | 30 |
| | References | 30 |

1 Introduction

Cluster states have garnered significant attention in quantum computation and information due to their role as universal resources for measurement-based quantum computation (MBQC) [1–3]. In contrast to the traditional circuit model, where unitary operations are applied sequentially, MBQC utilizes a highly entangled initial state—the cluster state—on which adaptive single-qubit measurements are performed to drive the computation [4]. This paradigm shift has been extensively studied, both theoretically and experimentally, highlighting the versatility and scalability of cluster states in quantum information processing [5, 6].

A particularly intriguing application of cluster states is their connection to topological quantum codes. Recently, significant progress has been made in realizing topologically ordered states on programmable quantum simulators [7, 8]. This approach offers an alternative method for constructing topologically ordered states within the MBQC framework, where logical operations are realized via carefully designed measurement protocols. The toric code, introduced by Kitaev, serves as a foundational model in topological quantum error correction, characterized by its intrinsic fault tolerance and anyonic excitations [9]. The interplay between MBQC and topological order underscores a profound link between quantum computation and condensed matter physics, motivating further exploration of cluster-state-based constructions of topological codes.

Building upon this foundation, we extend the \mathbb{Z}_2 cluster state framework to a \mathbb{Z}_3 cluster state and demonstrate that a \mathbb{Z}_3 toric code state can be achieved through a similar measurement-based process. This generalization is particularly compelling as higher-dimensional qudits, such as qutrits, have garnered interest for their potential to enhance computational power and robustness against certain errors. Moreover, by modifying the \mathbb{Z}_3 cluster state prior to measurement, we can obtain a deformed \mathbb{Z}_3 toric code, which interpolates between different topological phases. Previous studies have extensively examined the phase diagram of the de-

formed \mathbb{Z}_2 toric code, revealing insights into topological phase transitions [10]. In this work, we extend this analysis to the \mathbb{Z}_3 case, providing a systematic exploration of its phase diagram and the role of deformations in its topological properties.

The remainder of this paper is structured as follows. In Sec. 2.1, we introduce the formalism of the \mathbb{Z}_3 toric code and its relation to cluster states, outlining the measurement-based approach to generating topological states. In Sec. 3, we describe how a deformed \mathbb{Z}_3 toric code state can be constructed by modifying the \mathbb{Z}_3 cluster state and discuss its corresponding parent Hamiltonian. In Sec. 4, we analyze the phase diagram of the deformed \mathbb{Z}_3 toric code by considering different deformation parameters and their impact on topological order. In Sec. 5, we employ tensor network techniques to further investigate the nature of the deformed \mathbb{Z}_3 toric code, including its connection to the Ashkin-Teller-like classical model and its projected entangled pair state (PEPS) representation. Finally, in Sec. 6, we summarize our findings and discuss potential future directions.

2 Models

2.1 \mathbb{Z}_N Toric Code

The toric code Hamiltonian is given by:

$$H_{\text{TC}} = - \sum_v A_v - \sum_p B_p, \quad (1)$$

where v and p denote the vertices and plaquettes of the two-dimensional square lattice. The projection operators are defined as:

$$A_v = \sum_{n=0}^{N-1} (a_v)^n, \quad B_p = \sum_{n=0}^{N-1} (b_p)^n, \quad (2)$$

where the vertex and plaquette operators

$$a_v = \prod_{l \in v} Z_l^{\xi_l}, \quad b_p = \prod_{l \in p} X_l^{\zeta_l}. \quad (3)$$

Here, the signs $\xi_l = \pm 1$ and $\zeta_l = \pm 1$ are defined as illustrated in Fig. 1, and X_l and Z_l are the \mathbb{Z}_N generalized Pauli matrices defined on link l , satisfying $Z_l X_l = \omega X_l Z_l$ with $\omega^N = 1$. These matrices have eigenvalues $1, \omega, \dots, \omega^{N-1}$. It is straightforward to verify that the projection operators commute with each other, i.e., $[A_v, A_{v'}] = 0$, $[B_p, B_{p'}] = 0$, and $[A_v, B_p] = 0$. Consequently, the ground state is stabilized by the conditions $a_v = 1$ for all v and $b_p = 1$ for all p . An electric anyon excitation with charge a at v corresponds to $a_v = \omega^a$, while a magnetic anyon excitation with charge b at p corresponds to $b_p = \omega^b$, where $a, b = 0, \dots, N-1$. Notably, the model exhibits the electric-magnetic duality [11]:

$$\mathcal{D}_{\text{e-m}}: X \leftrightarrow Z, \quad \text{and} \quad v \leftrightarrow p. \quad (4)$$

On a torus, the model is characterized by two X holonomy operators defined as

$$W_X^x = \prod_{l \in \mathcal{C}_x} X_l, \quad \text{and} \quad W_X^y = \prod_{l \in \mathcal{C}_y} X_l, \quad (5)$$

where \mathcal{C}_x and \mathcal{C}_y represent non-contractible paths on the lattice that wind around the system in the x and y directions, respectively. Similarly, the model features two Z holonomies given

by

$$W_Z^x = \prod_{l \in \mathcal{C}'_x} Z_l, \quad \text{and} \quad W_Z^y = \prod_{l \in \mathcal{C}'_y} Z_l, \quad (6)$$

with \mathcal{C}'_x and \mathcal{C}'_y denoting non-contractible paths on the dual lattice winding in the x and y directions, respectively. These holonomy operators satisfy the following Heisenberg algebra:

$$W_Z^y W_X^x = \omega W_X^x W_Z^y, \quad \text{and} \quad W_Z^x W_X^y = \omega W_X^y W_Z^x. \quad (7)$$

Due to these Heisenberg commutation relations, the TC model exhibits a ground state degeneracy of N^2 .

One of the degenerate ground states can be constructed by applying the projection operator to a reference product state, as follows:

$$|\text{TC}_N\rangle = \prod_p B_p |\mathbf{0}\rangle. \quad (8)$$

Here, $|\mathbf{0}\rangle = \otimes_i |0\rangle$, where $|0\rangle$ is the local qudit state satisfying $Z|0\rangle = |0\rangle$. This state is an eigenstate of both the W_Z^x and W_Z^y holonomies, each with eigenvalue 1. The other ground states, expressed in the basis of the W_X^y and W_X^x holonomies, are given by:

$$|\text{TC}_N\rangle = \sum_{i,j=0}^{N-1} (W_X^y)^i (W_X^x)^j \prod_p B_p |\mathbf{0}\rangle, \quad (9)$$

which is an eigenstate of the W_X^y and W_X^x holonomies, each with eigenvalue 1.

In this work, we use either expression from Eqs. (8) or (9) interchangeably, depending on the context, and focus on analyzing the quantum phases and their associated topological properties that emerge through deformation. The choice of basis does not significantly impact the overall argument.

2.2 Cluster State: Toric Code Ground State

The cluster state serves as a significant resource in quantum information and topological matter [3, 12]. In particular, it has been demonstrated that the TC state can be obtained by applying appropriate measurements to the cluster state [7, 8]. Here, we discuss how to generate the \mathbb{Z}_2 TC state from the cluster state through specific measurement protocols and extend this approach to generalize the generation of the \mathbb{Z}_3 TC state.

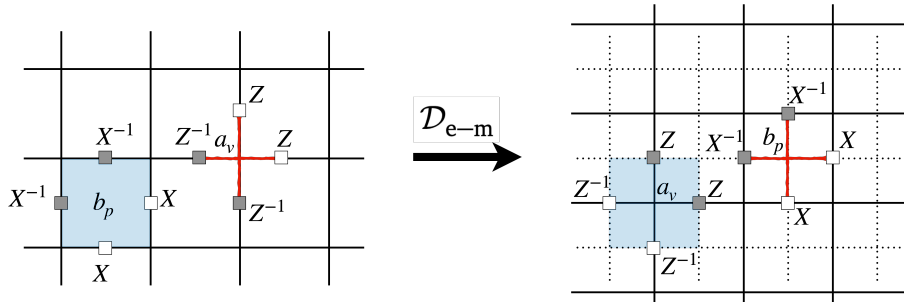


Figure 1: (Left panel) Vertex and plaquette stabilizers, a_v and b_p , in the toric code model. (Right panel) The lattice and stabilizers following the dual transformation \mathcal{D}_{e-m} . The original lattice is shown with dotted lines, while the dualized lattice is depicted with solid lines.

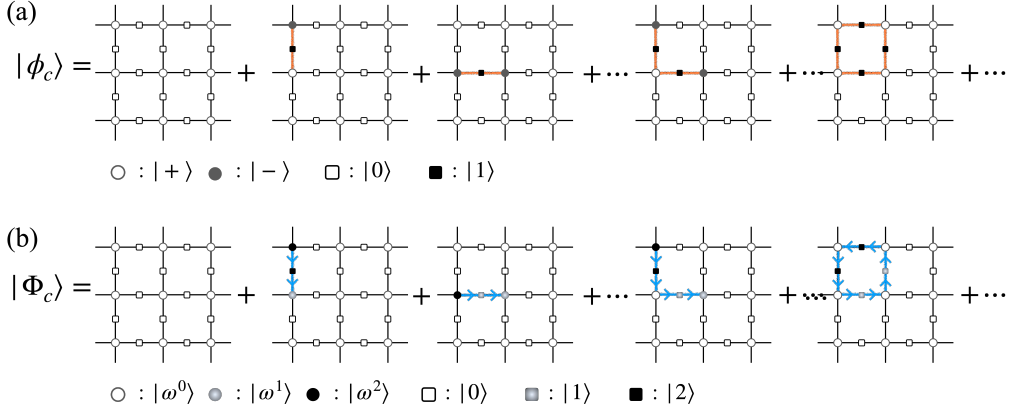


Figure 2: Expansion of the cluster state on the Lieb lattice for (a) the \mathbb{Z}_2 case and (b) the \mathbb{Z}_3 case. Each term in the product of Eq. (10) (or Eq. (12)) corresponds to a dimer configuration. In (a), empty circles and squares represent $|+\rangle$ and $|0\rangle$, while filled ones represent $|-\rangle$ and $|1\rangle$; orange lines denote links where $Z_{v_l}X_lZ_{v'_l}$ is applied. In (b), circles and squares with three shadings represent the \mathbb{Z}_3 eigenstates $|\omega^0\rangle$, $|\omega^1\rangle$, $|\omega^2\rangle$ and $|0\rangle$, $|1\rangle$, $|2\rangle$, respectively; blue arrows indicate the direction of the ZXZ dimers.

We begin with the \mathbb{Z}_2 cluster state defined on Lieb lattice as follows:

$$|\phi_2\rangle = \left[\prod_l (I + Z_{v_l}X_lZ_{v'_l}) \right] |+\rangle^{\otimes v} |0\rangle^{\otimes l}, \quad (10)$$

where v_l and v'_l are neighboring vertices connected by the link l , $|0\rangle^{\otimes l} \equiv \otimes_l |0_l\rangle$, and $|+\rangle^{\otimes v} \equiv \otimes_v |+_v\rangle$ with $|+_v\rangle$ being an eigenstate of X_v . In a quantum circuit, the cluster state can be prepared by applying controlled-Z (CZ) gates to neighboring qubits residing on the Lieb lattice [3].

Interpreting $Z_{v_l}X_lZ_{v'_l}$ as a dimer on the link l , the expansion of the product over l in Eq. (10) results in an equal-weight superposition of all possible dimer configurations, including those that allow vertices to be shared, as illustrated in Fig. 2 (a); empty circles and squares represent $|+\rangle$ and $|0\rangle$, respectively, while filled circles and squares represent the states $|-\rangle$ and $|1\rangle$. The orange lines denote the links where the operator $Z_{v_l}X_lZ_{v'_l}$ has been applied.

The operation of $Z_{v_l}X_lZ_{v'_l}$ flips the local qubits in its support as $|0\rangle \leftrightarrow |1\rangle$ and $|+\rangle \leftrightarrow |-\rangle$. Therefore, the qubit state on the link l occupied by the dimer is $|1\rangle$, while the one on the vertex v shared by an odd (even) number of dimers is $|-\rangle$ ($|+\rangle$). As a result, the states with the dimers forming closed loops do not contain the $|-\rangle$ state on any vertex. By performing a forced measurement on the vertex qubits in the $|+\rangle$ state, only configurations with closed loops remain, where the link qubits on the loops are in the $|1\rangle$ state, while all other link qubits are in the $|0\rangle$ state. This resulting state corresponds to the ground state of the \mathbb{Z}_2 toric code:

$$|\text{TC}_2\rangle \propto (\langle + |)^{\otimes v} |\phi_2\rangle = \sum_{c_i} |c_i\rangle, \quad (11)$$

which is equivalent to the state in Eq. (9). Here, the summation runs over all possible closed-loop configurations c_i of $|1\rangle$ states in the background of $|0\rangle$ state.

The protocol can be naturally extended to the \mathbb{Z}_N TC state using the \mathbb{Z}_N cluster state and suitable measurement schemes. In particular, for the \mathbb{Z}_3 case, the cluster state is defined as:

$$|\phi_3\rangle = \left[\prod_l (I + Z_{v_l}^\dagger X_l Z_{v'_l} + Z_{v_l} X_l^\dagger Z_{v'_l}^\dagger) \right] |\omega^0\rangle^{\otimes v} |0\rangle^{\otimes l}. \quad (12)$$

Here, $|0\rangle^{\otimes l} \equiv \otimes_l |0\rangle_l$, with $|0\rangle$ being the eigenstate of the \mathbb{Z}_3 operator Z_l , and $|\omega^0\rangle^{\otimes v} \equiv \otimes_v |\omega_v^0\rangle$, where $|\omega_v^0\rangle$ is the eigenstate of the \mathbb{Z}_3 operator X_v . Note that v_l refers to the vertex located left (down) from l , and v'_l refers to the vertex located right (up) from l .

Similar to the \mathbb{Z}_2 case, we consider the ZXZ operation as a dimer, but now there are two distinct types. As will be shown, it is useful to distinguish these dimers by assigning them a direction: the rightward (upward) dimer $Z_{v_l}^\dagger X_l Z_{v'_l}$, and the leftward (downward) dimer $Z_{v'_l} X_l^\dagger Z_{v_l}^\dagger$. Consequently, expanding the product over l in Eq. (12) generates a superposition of all possible two-species dimer configurations as depicted in Fig. 2 (b). Here, the empty circles and squares correspond to $|\omega^0\rangle$ and $|0\rangle$, respectively, while the circles and squares filled in gray represent $|\omega^1\rangle$ and $|1\rangle$, and those filled in black represent $|\omega^2\rangle$ and $|2\rangle$. Then, the vertex qutrits take the state $|\omega^{n_v}\rangle$, where $n_v \equiv n_v^{\text{in}} - n_v^{\text{out}}$, with n_v^{in} and n_v^{out} denoting the number of dimers incoming to and outgoing from the vertex, respectively.

Performing a forced measurement on vertices in the state $|\omega^0\rangle_v$ leaves only the closed \mathbb{Z}_3 loop configurations, corresponding to configurations where $n_v = 0$ for all vertices. The resulting state can be interpreted as an equal-weight superposition of all possible domain-wall configurations of the 3-state Potts model, where the link qutrits are in $|1\rangle$ or $|2\rangle$, depending on the direction of the domain wall, against a background of $|0\rangle$. Indeed, this corresponds to the \mathbb{Z}_3 TC state:

$$|\text{TC}_3\rangle \propto (\langle \omega^0 |)^{\otimes v} |\phi_3\rangle = \sum_{c_i} |c_i\rangle, \quad (13)$$

where $|c_i\rangle$ denotes a certain domain-wall configuration. In each configuration, the states on links unoccupied by any loops correspond to $|0\rangle$, the states on links with direction aligned with the positive coordinate axis correspond to $|1\rangle$, and the states on links with direction aligned with the negative coordinate axis correspond to $|2\rangle$.

3 Generating Deformed \mathbb{Z}_3 Toric Code

In this section, we describe the deformation protocol applied to the \mathbb{Z}_3 cluster state, which, following the same measurement protocol discussed in the previous section, results in a deformed \mathbb{Z}_3 TC state. Then, we recast the deformed TC state into an alternative basis, enabling a more straightforward and insightful analysis. Finally, we derive the parent Hamiltonian that hosts the deformed \mathbb{Z}_3 TC states as its ground states.

3.1 Deformed \mathbb{Z}_3 Cluster State

We begin with defining a rotated qutrit state as follows:

$$|0\rangle \rightarrow |\theta^0\rangle \equiv \cos \theta |0\rangle + \frac{\sin \theta}{\sqrt{2}} (|1\rangle + |2\rangle). \quad (14)$$

Here, $|0\rangle$, $|1\rangle$, and $|2\rangle$ are eigenstates of the \mathbb{Z}_3 operator Z with eigenvalues 1, ω , and ω^2 , respectively, where $\omega^3 = 1$. The state $|\theta^0\rangle$ can be prepared by applying an appropriate unitary operator to $|0\rangle$. We consider the above $|\theta^0\rangle$ state as one of the basis states. To preserve the algebra, i.e., ensuring that the operator X permutes the basis states, we define the remaining two basis states as follows:

$$\begin{aligned} |\theta^1\rangle &\equiv X|\theta^0\rangle = \cos \theta |1\rangle + \frac{\sin \theta}{\sqrt{2}} (|2\rangle + |0\rangle), \\ |\theta^2\rangle &\equiv X^2|\theta^0\rangle = \cos \theta |2\rangle + \frac{\sin \theta}{\sqrt{2}} (|0\rangle + |1\rangle). \end{aligned} \quad (15)$$

Each of the three states $|\theta^0\rangle$, $|\theta^1\rangle$, and $|\theta^2\rangle$ is normalized to 1, but they are not mutually orthogonal:

$$\langle\theta^a|\theta^b\rangle = \sin\theta \left(\frac{1}{2} \sin\theta + \sqrt{2} \cos\theta \right), \quad \text{for } a \neq b. \quad (16)$$

The basis states can be visualized as vectors in the three-dimensional vector space, each forming an angle of θ with the z -axis and rotated by 120° around the $[111]$ -axis relative to each other, as illustrated in Fig. 3. Note that the overlap between the rotated basis states, $\langle\theta^a|\theta^b\rangle$, varies from $-\frac{1}{2}$ to 1 as θ changes. When $\langle\theta^a|\theta^b\rangle = 0$ ($\theta = 0$), the three states form an orthonormal basis spanning the three-dimensional Hilbert space. When $\langle\theta^a|\theta^b\rangle = -\frac{1}{2}$ ($\theta = \frac{\pi}{2}$), the three states lie within a two-dimensional Hilbert subspace (or a plane in the three-dimensional vector space). In contrast, when $\langle\theta^a|\theta^b\rangle = 1$ ($\theta = \arctan \frac{\sqrt{3}-1}{\sqrt{2}}$), all three states become identical, collapsing into a single state.

Now, our deformation protocol is straightforward: we smoothly rotate the link qutrits $|\mathbf{0}\rangle^{\otimes l}$ in the reference state into the rotated one $|\theta^0\rangle^{\otimes l} \equiv \otimes_l |\theta_l^0\rangle$, resulting in the deformed cluster state:

$$|\phi_3(\theta)\rangle = \prod_l \left(I + Z_{v_l}^\dagger X_l Z_{v_l'} + Z_{v_l} X_l^\dagger Z_{v_l'}^\dagger \right) |\omega^0\rangle^{\otimes v} |\theta^0\rangle^{\otimes l}. \quad (17)$$

By performing a forced measurement on the vertex qutrits in the state $\langle\omega^0|^{\otimes v}$, the resulting state is given as:

$$|\Psi_3(\theta)\rangle = (\langle\omega^0|^{\otimes v} |\phi_3(\theta)\rangle) = \sum_{\vec{c}_i} |\vec{c}_i\rangle. \quad (18)$$

Since the vertex qutrits remain unchanged before the measurement, the geometrical interpretation of $|\Psi_3(\theta)\rangle$ is preserved as the equal-weight superposition of domain-wall configurations of the 3-state Potts model. The difference is that $|0\rangle \rightarrow |\theta^0\rangle$ on unoccupied sites, and $|1\rangle \rightarrow |\theta^1\rangle$, $|2\rangle \rightarrow |\theta^2\rangle$ on loops, depending on the direction. It is noteworthy that two different loop configurations are no longer orthogonal.

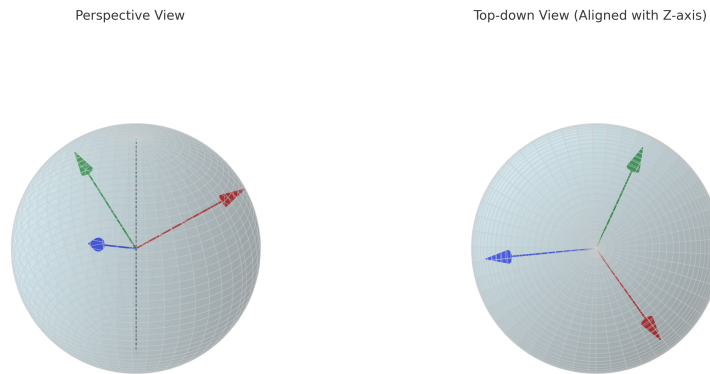


Figure 3: Visualization of the rotated basis states $|\theta^0\rangle$, $|\theta^1\rangle$, and $|\theta^2\rangle$ as vectors in the three-dimensional vector space. (Left) Perspective view showing the three vectors tilted at an angle θ from the z -axis. (Right) Top-down view along the z -axis, highlighting the 120° rotational symmetry about the $[111]$ -axis. As θ varies, the mutual overlap $\langle\theta^a|\theta^b\rangle$ interpolates between $-\frac{1}{2}$ (coplanar) and 1 (collinear), with 0 (orthonormal) at $\theta = 0$.

3.2 Deformed Toric Code State and Parent Hamiltonian

The deformed \mathbb{Z}_3 TC state $|\Psi_3(\theta)\rangle$, derived from the deformed cluster state, is equivalent to applying a filtering operation directly on the \mathbb{Z}_3 TC state:

$$|\tilde{\Psi}(\beta_x)\rangle \equiv \prod_l e^{\frac{\beta_x}{2}\Gamma_l^x} |\text{TC}_3\rangle, \quad \text{where} \quad \Gamma^x = \begin{pmatrix} -1 & 2 & 2 \\ 2 & -1 & 2 \\ 2 & 2 & -1 \end{pmatrix}. \quad (19)$$

The local deformation operator $D_l(\beta_x) = \exp\left(\frac{\beta_x}{2}\Gamma^x\right)$ transforms the local basis states as follows:

$$\begin{aligned} |0\rangle &\xrightarrow{D(\beta_x)} |\tilde{0}\rangle \propto \left(3 - \tanh\frac{\beta_x}{2}\right)|0\rangle + 2\tanh\frac{\beta_x}{2}(|1\rangle + |2\rangle), \\ |1\rangle &\xrightarrow{D(\beta_x)} |\tilde{1}\rangle \propto \left(3 - \tanh\frac{\beta_x}{2}\right)|1\rangle + 2\tanh\frac{\beta_x}{2}(|0\rangle + |2\rangle), \\ |2\rangle &\xrightarrow{D(\beta_x)} |\tilde{2}\rangle \propto \left(3 - \tanh\frac{\beta_x}{2}\right)|2\rangle + 2\tanh\frac{\beta_x}{2}(|0\rangle + |1\rangle). \end{aligned} \quad (20)$$

Therefore, with proper normalization, one finds that $|\tilde{0}\rangle$, $|\tilde{1}\rangle$, and $|\tilde{2}\rangle$ are equivalent to $|\theta^0\rangle$, $|\theta^1\rangle$, and $|\theta^2\rangle$, as defined in Eqs. (14) and (15). The overlap between any two states is given by:

$$\langle \tilde{a} | \tilde{b} \rangle = \frac{4 \tanh\left(\frac{\beta_x}{2}\right)}{3 \tanh^2\left(\frac{\beta_x}{2}\right) - 2 \tanh\left(\frac{\beta_x}{2}\right) + 3}. \quad (21)$$

As β_x varies from $-\infty$ to ∞ , the value of $\langle \tilde{a} | \tilde{b} \rangle$ changes from $-\frac{1}{2}$ to 1. At $\langle \tilde{a} | \tilde{b} \rangle = 0$, the three states form an orthonormal basis spanning the three-dimensional space. When $\langle \tilde{a} | \tilde{b} \rangle = -\frac{1}{2}$, the states are restricted to a two-dimensional subspace, and when $\langle \tilde{a} | \tilde{b} \rangle = 1$, all three states collapse into a single vector.

The deformed states $|\tilde{0}\rangle$, $|\tilde{1}\rangle$, and $|\tilde{2}\rangle$ share characteristics with the states $|\theta^0\rangle$, $|\theta^1\rangle$, and $|\theta^2\rangle$ from Eqs. (14) and (15), particularly in terms of the angles between them. By appropriately mapping the parameters β_x and θ , the states $|\theta^0\rangle$, $|\theta^1\rangle$, and $|\theta^2\rangle$ can be related to the deformed states $|\tilde{0}\rangle$, $|\tilde{1}\rangle$, and $|\tilde{2}\rangle$.

Thus, the wavefunction $|\Psi_3(\theta)\rangle$ in Eq. (18) is equivalent to the deformed \mathbb{Z}_3 toric code state, which we hereafter denote as $|\tilde{\Psi}(\beta_x)\rangle$:

$$|\tilde{\Psi}(\beta_x)\rangle = \prod_l D_l(\beta_x) |\text{TC}_3\rangle = \sum_{c_i} \prod_l D_l(\beta_x) |c_i\rangle = \sum_{c_i} |\tilde{c}_i\rangle. \quad (22)$$

Under the dual transformation defined in Eq. (4), the deformed toric code state transforms as:

$$|\tilde{\Psi}(\beta_z)\rangle = \prod_l D_l(\beta_z) |\text{TC}_3\rangle = \sum_{c_i} |\tilde{c}_i\rangle, \quad (23)$$

where $\beta_x \rightarrow \beta_z$, and the deformation operator $D_l(\beta_z)$ is expressed as:

$$D_l(\beta_z) = \exp\left(\frac{\beta_z}{2}\Gamma_l^z\right) \propto I_l + \tanh\left(\frac{\beta_z}{2}\right)\Gamma_l^z, \quad \text{where} \quad \Gamma^z = U_{X \leftrightarrow Z} \Gamma^x U_{X \leftrightarrow Z}^\dagger = \begin{pmatrix} 1 & 0 & 0 \\ 0 & -1 & 0 \\ 0 & 0 & -1 \end{pmatrix}. \quad (24)$$

Consequently, our deformation protocol can be interpreted as tuning the loop fugacity through the parameter θ or β_z , where the fugacity per link becomes $e^{-\beta_z}$. This breaks the equal-weight configuration characteristic of the TC state, filtering a specific channel determined by the parameter θ or β_z .

Under the Γ^z deformation, the three local states $|0\rangle$, $|1\rangle$, and $|2\rangle$ in $|\tilde{c}\rangle$ transform as:

$$|0\rangle \rightarrow |\tilde{0}\rangle = |0\rangle, \quad |1\rangle \rightarrow |\tilde{1}\rangle = \exp(-\beta_z)|1\rangle, \quad |2\rangle \rightarrow |\tilde{2}\rangle = \exp(-\beta_z)|2\rangle. \quad (25)$$

The parent Hamiltonian, whose ground state corresponds to Eq. (23), is given by:

$$H'_{\text{TC}} = H_{\text{TC}} + \sum_p (C_{p,1} + C_{p,2}). \quad (26)$$

Here the operators $C_{p,1}$ and $C_{p,2}$ are defined as:

$$C_{p,1} = \begin{array}{c} \Sigma_2 \\ \square \\ \Sigma_1 \end{array}, \quad C_{p,2} = \begin{array}{c} \Sigma_1 \\ \square \\ \Sigma_2 \end{array}, \quad (27)$$

where

$$\Sigma^1 = \begin{pmatrix} e^{\beta_z} & 0 & 0 \\ 0 & e^{-\beta_z} & 0 \\ 0 & 0 & 1 \end{pmatrix}, \quad \Sigma^2 = \begin{pmatrix} e^{\beta_z} & 0 & 0 \\ 0 & 1 & 0 \\ 0 & 0 & e^{-\beta_z} \end{pmatrix}. \quad (28)$$

One can verify that $|\tilde{\Psi}(\beta_z)\rangle$ is the ground state of H'_{TC} by showing that the additional terms $C_{p,1}$ and $C_{p,2}$ annihilate the deformed state while preserving the stabilizer conditions of the original toric code Hamiltonian.

One can summarize the contents of this section as follows:

- We introduced a cluster-like state $|\phi_3(\theta)\rangle$ constructed by applying a rotation operator to the vacuum configuration:

$$|+_v\rangle \otimes |0_l\rangle \rightarrow |+_v\rangle \otimes |\theta_l^0\rangle.$$

- By performing forced measurements on the vertex states, we obtained the state $|\Psi_3(\theta)\rangle$.
- We showed that the same state can be equivalently constructed by applying the deformation operator $D_l(\beta_x)$ to the toric code wavefunction:

$$|\tilde{\Psi}(\beta_x)\rangle = \prod_l D_l(\beta_x)|\text{TC}_3\rangle.$$

- Through the dual transformation \mathcal{D}_{e-m} , the wavefunction is mapped to $|\tilde{\Psi}(\beta_z)\rangle$, and the explicit form of the parent Hamiltonian H'_{TC} is derived.

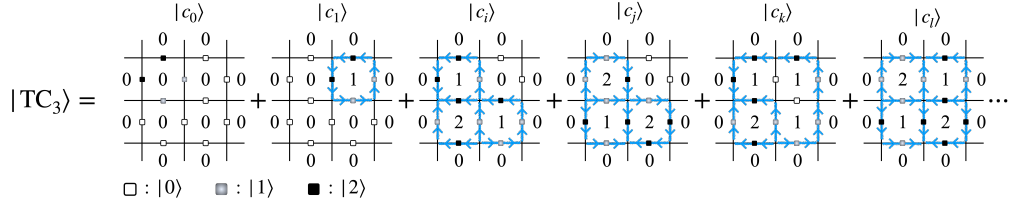


Figure 4: Loop-gas representation of the \mathbb{Z}_3 toric code ground state $|TC_3\rangle$ as an equal superposition of closed-loop configurations $|c_i\rangle$. The numbers at the center of each plaquette indicate how many times (mod 3) the operator b_p has been applied. Blue arrows denote directed loops: links with rightward (downward) arrows carry $|1\rangle$, links with leftward (upward) arrows carry $|2\rangle$, and unoccupied links correspond to $|0\rangle$. Empty, gray, and black squares represent the local states $|0\rangle$, $|1\rangle$, and $|2\rangle$, respectively.

4 Phase Diagram of Deformed \mathbb{Z}_3 Toric Code

4.1 Phase Diagram of $|\tilde{\Psi}(\beta_z)\rangle$

4.1.1 Loop and Net Description

To analyze the phase diagram of the deformed \mathbb{Z}_3 toric code (TC), the loop-gas configuration representation serves as an essential tool. As expressed in Eq. (22), the ground state of the \mathbb{Z}_3 TC can be written as an equal superposition of all possible closed-loop configurations:

$$|TC_3\rangle = \sum_{c_i} |c_i\rangle. \quad (29)$$

These configurations are connected by the group G , which is generated by the operators b_p and b_p^2 . Starting from the fully magnetized configuration $|0\rangle = \prod_l |0\rangle_l$, where $|0\rangle_l$ is the eigenstate of Z_l with eigenvalue +1, all other configurations can be obtained by applying elements $g \in G$.

This representation is depicted in Fig. 4, which highlights two distinct types of loops differentiated by directional arrows. The numbers at the center of each plaquette indicate how many times (mod 3) the b_p operator has been applied to transition from $|0\rangle$ to the given configuration. Loops form between neighboring plaquettes with differing numbers: a difference of $1 \pmod 3$ produces arrows pointing right (or downward), while a difference of $2 \pmod 3$ results in arrows pointing left (or upward). Links associated with rightward (or downward) arrows correspond to the local state $|1\rangle$, links with leftward (or upward) arrows correspond to $|2\rangle$, and links unoccupied by loops correspond to $|0\rangle$.

The charge of an e anyon at a vertex v is determined by the net divergence (mod 3) of the loops at that site. In the ground state, all configurations satisfy the divergence-free condition, ensuring that the total divergence at each vertex is zero (mod 3). e anyons are created in pairs by cutting loops in the ground-state configurations, leading to two vertices with opposite e -anyon charges at the endpoints of the open loop.

More specifically, a pair of e anyons can be created by flipping the local states along an open path γ that starts at vertex i and ends at vertex j :

$$\hat{O}_\gamma = \prod_{l \in \gamma} X_l^{\xi_l}, \quad (30)$$

where $\xi_l = \pm 1$ denotes the direction of the path γ on the link l . Applying \hat{O}_γ generates an

e -anyon pair state:

$$|e_i \bar{e}_j\rangle = \hat{O}_\gamma |TC_3\rangle = \sum_{c_i} \hat{O}_\gamma |c_i\rangle = \sum_{c_i} |c'_i\rangle. \quad (31)$$

In this expression, each configuration $|c'_i\rangle$ contains an open loop connecting vertices i and j , whose specific form depends on the original configuration $|c_i\rangle$. The resulting set of configurations encompasses all possible open loops that connect i and j .

At the toric code point, corresponding to the $\beta_z \rightarrow 0$ limit, the e anyon pairs are deconfined. This can be verified by evaluating:

$$\langle e_i \bar{e}_j | e_i \bar{e}_j \rangle = \sum_{c_i} \langle c'_i | c'_i \rangle. \quad (32)$$

At the toric code point, all overlaps $\langle c'_i | c'_i \rangle$ between e -anyon pair configurations contribute equally to the summation. This equality arises because the closed loops in the original configurations $|c\rangle$ are scale-invariant, leading to uniform normalization across all configurations $|c'_i\rangle$. Consequently, the overlap $\langle e_i \bar{e}_j | e_i \bar{e}_j \rangle$ is independent of the separation $|i - j|$ between e_i and \bar{e}_j , indicating that the e anyons are deconfined.

Since the open loop connecting vertices i and j can be obtained by cutting the closed loops in the original loop configurations $|c_i\rangle$, the confinement of open loops is directly linked to the confinement of closed loops. Under the general β_z deformation introduced in Eq. (23), each deformed loop configuration $|\tilde{c}_i\rangle$ is related to the bare configuration $|c\rangle$ through the assignment of a weight as follows:

$$|c\rangle \rightarrow |\tilde{c}_i\rangle = \exp(-\beta_z l_{c_i}) |c_i\rangle, \quad (33)$$

where l_{c_i} denotes the total length of loops in the configuration $|c\rangle$.

$$\langle \Psi(\beta_z) | \Psi(\beta_z) \rangle = \begin{array}{c} \langle \tilde{c}_0 | \tilde{c}_0 \rangle \\ \begin{array}{|c|c|c|c|} \hline 0 & 0 & 0 & 0 \\ \hline 0 & 0 & 0 & 0 \\ \hline 0 & 0 & 0 & 0 \\ \hline 0 & 0 & 0 & 0 \\ \hline \end{array} + \begin{array}{c} \langle \tilde{c}_1 | \tilde{c}_1 \rangle \\ \begin{array}{|c|c|c|c|} \hline 0 & 0 & 0 & 0 \\ \hline 1 & 0 & 0 & 0 \\ \hline 0 & 0 & 0 & 0 \\ \hline 0 & 0 & 0 & 0 \\ \hline \end{array} + \begin{array}{c} \langle \tilde{c}_2 | \tilde{c}_2 \rangle \\ \begin{array}{|c|c|c|c|} \hline 0 & 0 & 0 & 0 \\ \hline 0 & 1 & 0 & 0 \\ \hline 0 & 2 & 1 & 0 \\ \hline 0 & 0 & 0 & 0 \\ \hline \end{array} + \begin{array}{c} \langle \tilde{c}_3 | \tilde{c}_3 \rangle \\ \begin{array}{|c|c|c|c|} \hline 0 & 0 & 0 & 0 \\ \hline 0 & 2 & 0 & 0 \\ \hline 0 & 1 & 2 & 0 \\ \hline 0 & 0 & 0 & 0 \\ \hline \end{array} + \begin{array}{c} \langle \tilde{c}_k | \tilde{c}_k \rangle \\ \begin{array}{|c|c|c|c|} \hline 0 & 0 & 0 & 0 \\ \hline 0 & 1 & 1 & 0 \\ \hline 0 & 2 & 1 & 0 \\ \hline 0 & 0 & 0 & 0 \\ \hline \end{array} + \begin{array}{c} \langle \tilde{c}_l | \tilde{c}_l \rangle \\ \begin{array}{|c|c|c|c|} \hline 0 & 0 & 0 & 0 \\ \hline 0 & 2 & 1 & 0 \\ \hline 0 & 1 & 2 & 0 \\ \hline 0 & 0 & 0 & 0 \\ \hline \end{array} \dots \end{array}$$

Figure 5: Net configurations arising from the overlap $\langle \tilde{\Psi}(\beta_z) | \tilde{\Psi}(\beta_z) \rangle$ under the β_z deformation. Each overlap $\langle \tilde{c}_i | \tilde{c}_i \rangle$ is computed from the corresponding loop configuration in Fig. 4. The directional information of the loops is lost in the overlap, yielding undirected orange nets that may include branching points. The \mathbb{Z}_3 numbers on the plaquettes correspond to classical spin variables in the mapping to the $Q = 3$ Potts model.

To determine whether the closed loops are confined or deconfined under the deformation, one can compute the norm of the wavefunction $\langle \tilde{\Psi}(\beta_z) | \tilde{\Psi}(\beta_z) \rangle$, expressed as:

$$\langle \tilde{\Psi}(\beta_z) | \tilde{\Psi}(\beta_z) \rangle = \sum_c \langle \tilde{c} | \tilde{c} \rangle = \sum_N \chi_N(3) \exp(-\beta_z l_N). \quad (34)$$

Here, $\langle \tilde{c} | \tilde{c} \rangle$ represents the overlap of a single configuration, which is reformulated in terms of net configurations, as depicted in Fig. 5. Note that, only the overlaps between the same configuration contribute to the summation due to the orthogonality of the configurations. In this overlap, the directional information from loops is discarded, resulting in nets that may include branching. Consequently, the summation over loop configurations translates to a summation over net configurations N , where l_N is the total length of the net, and $\chi_N(3)$ represents the

number of loop configurations that correspond to the same net. This mapping is intrinsically connected to the chromatic polynomial $\chi_N(Q)$, which counts the number of ways to color the net N using Q distinct colors. For instance, Fig. 5 demonstrates how the overlap of different loop configurations can yield the same net, necessitating a combinatorial enumeration of all loop configurations contributing to that net.

Determining whether the loops in the original loop configurations are confined naturally translates to examining the confinement of nets in the net configurations described by Eq. (34). From the discussion earlier one can deduce that in the absence of deformation, the e -anyon pair creation operator generates open nets of varying lengths within the overlap configuration $\langle \tilde{c} | \tilde{c} \rangle$. In this deconfined phase, the contributions of all net configurations to the overlap are independent of the lengths of the open nets.

When a length-dependent weight is introduced, however, the contribution of each net configuration becomes sensitive to the length of the open nets. Beyond a certain point, the nets undergo a transition to a confined phase, making it progressively harder to separate the e -anyons created by the pair creation operator. This transition directly results in the confinement of the e -anyons.

4.1.2 Mapping to Classical Potts Model

The confinement behavior of the nets described in Eq. (34) can be analyzed by mapping the problem to a classical $Q = 3$ Potts model, characterized by the Hamiltonian:

$$H_{\text{Potts}} = -J \sum_{\langle i,j \rangle} \delta_{s_i, s_j}, \quad (35)$$

where s_i represents a local \mathbb{Z}_3 spin variable. The energy of a given configuration is determined by the length of the domain walls separating regions with distinct spin values, which correspond to closed nets. Thus, the net configurations shown in Fig. 5 can be interpreted as classical Potts model configurations with excitations, where each local net excitation is weighted by a Boltzmann factor of $\exp(-\beta)$. In this framework, the partition function of the Potts model can be expressed as:

$$Z_{\text{Potts}} = \sum_N \chi_N(3) \exp(-\beta l_N), \quad (36)$$

where $\beta = J/T$, N denotes all possible closed-net configurations, l_N is the total length of the nets in a given configuration, and $\chi_N(Q)$ represents the chromatic polynomial.

By comparing Eqs. (34) and (36), it becomes evident that the norm of the deformed \mathbb{Z}_3 TC wavefunction maps directly to the classical partition function of the $Q = 3$ Potts model when the parameters are matched as $\beta_z = \beta$. The net configurations shown in Fig. 5 can also be interpreted as classical configurations of the $Q = 3$ Potts model, where the \mathbb{Z}_3 numbers assigned to the plaquettes correspond to classical spin variables.

The $Q = 3$ Potts model exhibits a global \mathbb{Z}_3 symmetry defined by the operation:

$$U_1 = \prod_i X_i^s, \quad (37)$$

where the local operator X_i^s cyclically rotates the classical spin s_i through the states $0 \rightarrow 1 \rightarrow 2 \rightarrow 0$. The phases of the Potts model are characterized by whether, and how, the global symmetry U_1 is spontaneously broken. The overall phase diagram of the $Q = 3$ Potts model, parameterized by $\exp(\beta)$, is illustrated in Fig. 6 [13]. Interestingly, this phase diagram includes the imaginary temperature regime where $\exp(\beta) < 0$. The real temperature regime is further subdivided into two distinct regions: the ferromagnetic (FM) regime with $J > 0$ and $\exp(\beta) \geq 1$, and the antiferromagnetic (AFM) regime with $J < 0$ and $0 \leq \exp(\beta) \leq 1$.

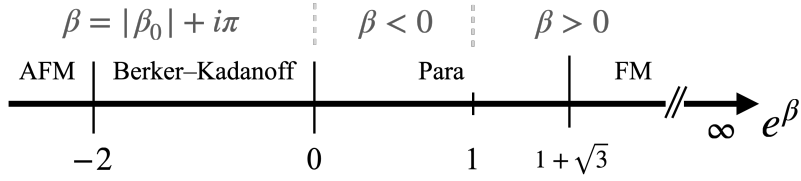


Figure 6: Phase diagram of the $Q = 3$ Potts model as a function of e^β . The ferromagnetic (FM) regime at $e^\beta > 1 + \sqrt{3}$ is separated from the paramagnetic (Para) phase by a critical point at $e^{\beta_c} = 1 + \sqrt{3}$, governed by a CFT with central charge $c = 4/5$. The antiferromagnetic (AFM) critical point at $e^\beta = -2$ corresponds to a \mathbb{Z}_4 parafermion CFT with $c = 1$. The intermediate Berker-Kadanoff phase occupies the region $-2 < e^\beta < 0$.

In the FM regime, the $Q = 3$ Potts model exhibits a phase transition at:

$$\exp(\beta_c) = 1 + \sqrt{3}. \quad (38)$$

This critical point is governed by a \mathbb{Z}_3 conformal field theory (CFT) with a central charge of $c = \frac{4}{5}$. For temperatures above the critical value ($\exp(\beta_z) < \exp(\beta_c)$), the system remains symmetric under U_1 , and the classical spins reside in a disordered paramagnetic phase. In this phase, nets representing domain walls proliferate throughout the ensemble. Notably, this disordered phase includes the toric code point at $\beta = 0$, which corresponds to the high-temperature limit of the classical system ($T \rightarrow \infty$).

As β increases from 0, corresponding to a decrease in the classical temperature T , the ensemble undergoes spontaneous symmetry breaking, and the classical spins gradually begin to align. This process continues until the system reaches the critical point at $\beta = \beta_c$. At this critical point, the system transitions into an ordered phase. In the ordered phase, where $\exp(\beta) > \exp(\beta_c)$, the classical spins become aligned, resulting in confined nets and, consequently, the confinement of e anyons.

In the AFM regime, where $\exp(\beta) < 1$, the classical system remains disordered, ensuring that the e anyons remain deconfined across the entire parameter range, except at the point $\exp(\beta) = 0$. This point corresponds to the $T = 0$ limit of the AFM $Q = 3$ Potts model and marks another critical point. At this critical point, the system is described by a \mathbb{Z}_4 parafermion CFT with a central charge of $c = 1$ [14], signifying a transition to the Beker-Kadanoff phase. While the parameter regime $\exp(\beta) < 0$ is inaccessible through the deformed wavefunction, the critical point exhibits intriguing properties that merit further exploration.

4.1.3 Emergent $U(1)$ 1-Form Symmetry and Hilbert Space Fragmentation

At the critical point $\exp(\beta_z) = 0$, the loop weight dominates in the deformed wavefunction $|\tilde{\Psi}(\beta_z \rightarrow -\infty)\rangle$, and configurations containing at least one unoccupied link ($|0\rangle$) are eliminated, leaving only fully packed configurations. These remaining configurations map to the 6-vertex model by associating $|1\rangle$ and $|2\rangle$ states with up (right) and down (left) arrows, respectively. At this point, all vertices in every configuration satisfy the “two-in-two-out” condition, making it equivalent to the square-ice model.

Configurations with plaquettes featuring clockwise or counterclockwise arrow arrangements are flippable, meaning they can transition to another configuration by flipping the direction of arrows in that plaquette using b_p or b_p^2 . Conversely, plaquettes where the arrows fail to form a closed cycle are unflippable.

Recent studies [15] show that the ensemble of 6-vertex model possesses an emergent $U(1)$ 1-form symmetry. At $\beta_z = -\infty$, the deformed wavefunction acquires this additional symmetry alongside the original 1-form symmetry of the parent Hamiltonian. In the PEPS representation

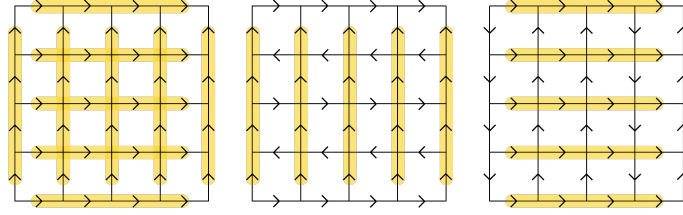


Figure 7: Examples of scar-state configurations at the square ice point $\exp(\beta_z) = 0$, where all vertices satisfy the two-in-two-out condition. Yellow shading highlights the links that are uniformly aligned in one direction (either all vertical or all horizontal). When all links along one lattice direction are aligned, every plaquette becomes unflippable under b_p and b_p^2 , resulting in configurations that are disconnected from the rest of the Hilbert space.

of the deformed wavefunction, this emergent $U(1)$ 1-form symmetry manifests as an injective symmetry of the local tensors. Detailed tensor network analysis is presented in Sec. 5.

The emergent $U(1)$ 1-form symmetry charge is defined by:

$$\hat{N}_C = \sum_{l_{\text{odd}} \in C} \hat{P}_l^1 - \sum_{l_{\text{even}} \in C} \hat{P}_l^2, \quad (39)$$

where C is a non-contractible closed path on the dual lattice, and $\hat{P}^a = |a\rangle\langle a|$ is a local projector. The operator \hat{N}_C measures the difference between the total number of $|1\rangle$ states on odd-numbered sites and $|2\rangle$ states on even-numbered sites along C .

This emergent symmetry fragments the Hilbert space, giving rise to “scar” state configurations whose number grows exponentially with the system size L under periodic boundary conditions. These configurations have no flippable plaquettes and exhibit the maximum absolute value of the symmetry charge, $\hat{N}_C = \pm L/2$. Examples of such configurations are illustrated in Fig. 7. Additional configurations can be constructed as follows. In the states shown in Fig. 7, either all vertical links or all horizontal links are aligned in the same direction, indicated by the yellow shading. When all links in either the vertical or horizontal direction are uniformly aligned, all plaquettes become unflippable. For example, if all vertical links are aligned, the L rows of links gain freedom to choose their directions independently. This results in 2^{L+1} configurations. Rotating the lattice by 90° produces 2^{L+1} additional configurations, all distinct from the original set. After accounting for overlaps, the total number of scar states is $2^{L+2} - 4$.

4.2 Phase Diagram of $|\tilde{\Psi}(\beta_x)\rangle$

4.2.1 Loop and Net Description

The dual wavefunction $|\tilde{\Psi}(\beta_x)\rangle$ can be analyzed in a similar fashion. In the limit $\beta_x \rightarrow 0$, the bare TC wavefunction emerges, where the local basis states $|0\rangle$, $|1\rangle$, and $|2\rangle$ remain orthonormal. As β_x increases, the orthonormality of the local basis is lost, as described by Eq. (21). In the opposite limit, $\beta_x \rightarrow \infty$, the three basis states align in the same direction, causing the loop configurations $\{|\tilde{c}_i\rangle\}$ to become indistinguishable. In this regime, e anyons are condensed, as creating an open loop in any configuration results in a state identical to the original.

More precisely, consider a loop configuration $|\tilde{c}\rangle$ and the configuration $|\tilde{c}'\rangle$ obtained by creating an e -anyon pair. The overlap $\langle \tilde{c} | \tilde{c}' \rangle$ becomes non-zero when β_x is finite. Along the path connecting the sites where anyons are created, i and j , the links correspond to the overlap of two distinct local states, $\langle \tilde{a} | \tilde{b} \rangle \equiv \nu$, where $a \neq b$. Without deformation, the overlap $\langle \tilde{c} | \tilde{c}' \rangle$ vanishes because the discrepancy line contributes $\nu = 0$. However, under β_x deformation, this contribution becomes non-zero, resulting in $\langle \tilde{c} | \tilde{c}' \rangle \neq 0$.

As a result, in the limit $\beta_x \rightarrow \infty$ (hence $\nu \rightarrow 1$), $\langle \tilde{\Psi}(\beta_x) | e_i \bar{e}_j \rangle \neq 0$, indicating that the e anyons are condensed. This occurs because the discrepancy lines become deconfined. The condensation of e anyons is directly tied to the proliferation of these discrepancy lines. At the phase transition point, located somewhere in the intermediate regime where the e anyons begin to condense, the discrepancy lines associated with $\mu = \langle a|b \rangle$ must also start to deconfine.

$$\langle \Psi(\beta_x) | \Psi(\beta_x) \rangle =$$

The figure displays two rows of diagrams representing the overlap of loop configurations. Each diagram is a 2x2 grid of plaquettes. The top row shows overlaps with the vacuum state $|c_0\rangle$, and the bottom row shows overlaps with $|c_1\rangle$. Each plaquette contains a pair of \mathbb{Z}_3 numbers (s_i, σ_i) . Green lines indicate discrepancy lines where the local overlap $\mu = \langle \tilde{a} | \tilde{b} \rangle$ ($a \neq b$) contributes. The diagrams are summed together to show the resulting net configurations.

Figure 8: Net configurations arising from the overlap $\langle \tilde{\Psi}(\beta_x) | \tilde{\Psi}(\beta_x) \rangle$ under the β_x deformation. The first row shows overlaps of all loop configurations with the vacuum state $|c_0\rangle$; the second row shows overlaps with $|c_1\rangle$. Each plaquette carries a pair of \mathbb{Z}_3 numbers (s_i, σ_i) from the ket and bra configurations. Green lines indicate discrepancy lines where the local overlap $\mu = \langle \tilde{a} | \tilde{b} \rangle$ ($a \neq b$) contributes. The two rows yield the same set of net configurations.

Discrepancy lines also appear in the overlap of two distinct closed loop configurations, $\langle \tilde{c}_i | \tilde{c}_j \rangle$, which becomes non-zero under the deformation β_x . Consequently, the overlaps of different configurations contribute to the norm of the deformed wavefunction:

$$\langle \tilde{\Psi}(\beta_x) | \tilde{\Psi}(\beta_x) \rangle = \sum_{c_i, c_j} \langle \tilde{c}_i | \tilde{c}_j \rangle. \quad (40)$$

As shown in Fig. 8, these discrepancy lines manifest as closed nets. Each plaquette now contains two numbers: one from the ket configuration and one from the bra configuration of the closed loops. The nets appear on the links that exhibit discrepancies in the local state overlaps, $\mu = \langle a|b \rangle$. The first and second rows in Fig. 8 depict the overlap configurations of all closed loop states with the states $|c_0\rangle$ and $|c_1\rangle$, respectively. Notably, the first and second rows yield the same set of net configurations.

In this way, the set of overlaps between any closed loop configuration $|c_i\rangle$ and all other configurations is equivalent to the set of overlaps between the vacuum state $|c_0\rangle$ and all configurations. Consequently, Eq. (40) can be expressed as:

$$\langle \tilde{\Psi}(\beta_x) | \tilde{\Psi}(\beta_x) \rangle = N_N \sum_N \chi_N(3) \mu^{l_N}. \quad (41)$$

Here, N_N denotes the total number of net configurations, l_N is the total length of the nets in a given configuration, and $\chi_N(Q)$ is the chromatic polynomial.

4.2.2 Mapping to Classical Potts Model

The analysis of whether the nets in Eq. (41) are confined or not also can be mapped to the study of classical $Q = 3$ Potts model as well. The norm of wavefunction can be mapped to

classical partition function in Eq. (36) by matching $\mu = \exp(-\beta)$.

Notably, by labeling the two digits on each plaquette in Fig. 8 as s_i and σ_i , the nets emerge as domain walls separating plaquettes where the difference between the two \mathbb{Z}_3 numbers, $s_i - \sigma_i$, is nonzero. Thus, each net configuration can be interpreted as a classical configuration of the $Q = 3$ Potts model by treating the difference of the two \mathbb{Z}_3 numbers, $S_i \equiv s_i - \sigma_i$, as a classical spin. The corresponding classical model is described by:

$$H'_{\text{Potts}} = -J' \sum_{\langle i,j \rangle} \delta_{S_i, S_j}, \quad (42)$$

This model exhibits a global \mathbb{Z}_3 symmetry defined by the operation:

$$U_2 = \prod_i X_i^s X_i^\sigma, \quad (43)$$

where the local operators X_i^s and X_i^σ cyclically rotate the classical spins s_i and σ_i through the states $0 \rightarrow 1 \rightarrow 2 \rightarrow 0$, respectively. The phases of the Potts model are characterized by whether, and how, the global symmetry U_2 is spontaneously broken.

The variational parameter μ spans the range $-\frac{1}{2}$ to 1. For nonzero values of $\mu \geq 0$, the corresponding classical system resides in the FM regime, where a phase transition occurs at:

$$\mu_c = \frac{1}{1 + \sqrt{3}}. \quad (44)$$

In the range $0 \leq \mu < \mu_c$, below this critical point, the classical system shows spontaneous symmetry breaking of U_2 and remains in an ordered phase, with the discrepancy lines suppressed. Consequently, the e anyons in the deformed toric code phase remain uncondensed within this parameter regime. Conversely, for $\mu_c < \mu \leq 1$, above the critical point, the classical system transitions to a disordered phase characterized by the proliferation of discrepancy lines. This transition results in the condensation of e anyons in the deformed toric code phase within this parameter range.

For negative values of μ , the classical system enters an imaginary temperature regime. In this case, the system exhibits AFM ordering, except at the second critical point $\mu_{c'} = -\frac{1}{2}$. Similar to the FM phase, the discrepancy lines are suppressed in the AFM phase, as they emerge as domain walls between plaquettes with differing S_i values. As a result, e anyons do not condense in this phase. Therefore, the phases of the deformed TC corresponding to the FM and AFM regimes, $\mu_{c'} < \mu < \mu_c$, can be regarded as belonging to the same phase.

4.2.3 Square Ice in Dual System

In the limit $\beta_x \rightarrow -\infty$ or $\mu = -\frac{1}{2}$, the system reaches a critical state described by \mathbb{Z}_4 parafermion conformal field theory (CFT). At this point, the three local vectors, $|\tilde{0}_l\rangle$, $|\tilde{1}_l\rangle$, and $|\tilde{2}_l\rangle$, lie in a two-dimensional subspace and are symmetrically related by rotations of $\frac{2\pi}{3}$. This relationship is captured by the condition $|\tilde{0}_l\rangle + |\tilde{1}_l\rangle + |\tilde{2}_l\rangle = 0$. Consequently, in this limit, the local Hilbert space required to describe the deformed wavefunction reduces from dimension 3 to dimension 2.

Under the \mathcal{D}_{e-m} duality mapping, the β_x -deformed wavefunction is transformed into a β_z -deformed wavefunction. At the dual point where $\beta_z \rightarrow -\infty$, the wavefunction corresponds to a fully packed loop state, with the local Hilbert space spanned by two orthonormal basis

states. Within this dual framework, the three local vectors transform as follows:

$$\begin{aligned} |\tilde{0}_l\rangle &\rightarrow |\tilde{\omega}_l^0\rangle = \frac{1}{\sqrt{3}} (|\tilde{0}_l\rangle + |\tilde{1}_l\rangle + |\tilde{2}_l\rangle) = 0, \\ |\tilde{1}_l\rangle &\rightarrow |\tilde{\omega}_l^1\rangle = \frac{1}{\sqrt{3}} (|\tilde{0}_l\rangle + \omega|\tilde{1}_l\rangle + \omega^2|\tilde{2}_l\rangle), \\ |\tilde{2}_l\rangle &\rightarrow |\tilde{\omega}_l^2\rangle = \frac{1}{\sqrt{3}} (|\tilde{0}_l\rangle + \omega^2|\tilde{1}_l\rangle + \omega|\tilde{2}_l\rangle), \end{aligned} \quad (45)$$

where $|\tilde{\omega}_l^1\rangle$ and $|\tilde{\omega}_l^2\rangle$ are orthonormal. Using this new basis, the original three vectors before the dual mapping can be expressed as:

$$\begin{aligned} |\tilde{0}_l\rangle &= \frac{\sqrt{2}}{2} (|\tilde{\omega}_l^1\rangle + |\tilde{\omega}_l^2\rangle), \\ |\tilde{1}_l\rangle &= \frac{\sqrt{2}}{2} (\omega^2|\tilde{\omega}_l^1\rangle + \omega|\tilde{\omega}_l^2\rangle), \\ |\tilde{2}_l\rangle &= \frac{\sqrt{2}}{2} (\omega|\tilde{\omega}_l^1\rangle + \omega^2|\tilde{\omega}_l^2\rangle). \end{aligned} \quad (46)$$

Since the dual local basis $|\tilde{\omega}^1\rangle$ and $|\tilde{\omega}^2\rangle$ span the two-dimensional local Hilbert space formed by the three deformed vectors $|\tilde{0}\rangle$, $|\tilde{1}\rangle$, and $|\tilde{2}\rangle$, the set of configurations of the dual lattice, $\{|\tilde{d}_i\rangle\}$, where every link is assigned the local basis $|\tilde{\omega}^1\rangle$ or $|\tilde{\omega}^2\rangle$, constitutes a complete set encompassing all configurations in $|\tilde{\Psi}(\beta_x \rightarrow -\infty)\rangle$. One can also interpret the dual configuration $|\tilde{d}_i\rangle$ as a loop configuration by treating $|\tilde{\omega}^1\rangle$ as representing an upward (or leftward) loop and $|\tilde{\omega}^2\rangle$ as representing a downward (or rightward) loop.

In the dual basis, the deformed wavefunction can be decomposed as

$$|\tilde{\Psi}(\beta_x \rightarrow -\infty)\rangle = \sum_j \left(\sum_i \langle \tilde{d}_i | \tilde{c}_j \rangle \right) |\tilde{d}_i\rangle. \quad (47)$$

Here, the overlap of configurations $\sum_j \langle \tilde{d}_i | \tilde{c}_j \rangle$ becomes zero when the dual loop configuration contains open loops. However, the overlaps with dual configurations composed entirely of closed loops are equal to each other.

To demonstrate this, consider the overlaps between the local vectors, which are given by:

$$\begin{aligned} \langle \tilde{\omega}^1 | \tilde{0} \rangle &= \langle \tilde{\omega}^2 | \tilde{0} \rangle = 1, \\ \langle \tilde{\omega}^1 | \tilde{1} \rangle &= \langle \tilde{\omega}^2 | \tilde{2} \rangle = \omega^2, && \text{(clockwise)} \\ \langle \tilde{\omega}^2 | \tilde{1} \rangle &= \langle \tilde{\omega}^1 | \tilde{2} \rangle = \omega. && \text{(counterclockwise)} \end{aligned} \quad (48)$$

As indicated above, the overlaps between the dual loop states and the original loop states become ω^2 when the direction of the dual loop corresponds to a clockwise 90° rotation of the original loop's direction. Similarly, the overlaps become ω when the dual loop's direction corresponds to a counterclockwise 90° rotation of the original loop's direction. The overlap between the dual loop state and the unoccupied original link state is 1.

Next, consider a loop in a certain configuration $|\tilde{d}_i\rangle$. In its overlap with the deformed wavefunction, we have

$$\langle \tilde{d}_i | \tilde{\Psi}(\beta_x \rightarrow -\infty) \rangle = \sum_j \langle \tilde{d}_i | \tilde{c}_j \rangle, \quad (49)$$

where the dual loop in $|\tilde{d}_i\rangle$ interacts with the original loops in $|\tilde{c}_j\rangle$. Focusing on the region supported by the dual loop under consideration, note that since the original loops are closed

by construction, any dual loop in closed form necessarily crosses each original closed loop twice—once in a clockwise direction and once in a counterclockwise direction. Consequently, the contribution of the dual loop to each $\langle \tilde{d}_i | \tilde{c}_j \rangle$ is 1.

On the other hand, when the dual loop under consideration has open ends, each end of the dual loop can be located within the interior of an original closed loop. This results in a single crossing, either clockwise or counterclockwise, contributing either ω^2 or ω to the overlap configuration. Since there exist an equal number of closed loop configurations where the closed loop enclosing the dual line ends is either absent or circulates in opposite directions, the contributions of these loops cancel out. Specifically, the overlaps with the dual open line yield 1, ω^2 , or ω , and the overall summation $\sum_j \langle \tilde{d}_i | \tilde{c}_j \rangle$ vanishes because $1 + \omega + \omega^2 = 0$. In other words, dual configurations containing an open dual line have zero overlap with the deformed wavefunction.

As a result, the deformed wavefunction in the limit of $\beta_x \rightarrow -\infty$ limit can be expressed by equal superposition of (fully packed) closed loop configuration as follows:

$$|\tilde{\Psi}(\beta_x \rightarrow -\infty)\rangle \propto \sum_i |\tilde{d}_i\rangle, \quad (50)$$

which is equivalent to the two-in-two-out configurations in Sec. 4.1.3.

5 Tensor Network Analysis

In the previous section, we introduced two types of deformations to the \mathbb{Z}_3 toric code (TC), labeled as β_x and β_z deformations. Utilizing the loop and net configuration framework, we analyzed the phase diagrams for each deformation. In each case, we identified phases where the e anyons are either condensed or confined, respectively. Additionally, in both cases, we observed a critical point exhibiting characteristics of the square ice model with an emergent $U(1)$ symmetry. Naturally, this raises questions about how the e -condensed and e -confined phases are connected, and what other phases might exist near the square ice critical point.

To address these questions, we introduce in this section a generalized deformed \mathbb{Z}_3 TC wavefunction characterized by two deformation parameters, β_x and β_z , and analyze it using the tensor network (TN) methodology. By expressing the norm of the wavefunction as a product involving a one-dimensional transfer matrix, we reveal that one of the holonomy operators acts as a global symmetry of the 1D system described by this transfer matrix. The breaking of this global symmetry is directly linked to the condensation or confinement of the e anyons. Furthermore, at the square ice critical point, an emergent $U(1)$ symmetry appears as an additional global symmetry.

This section is organized as follows: We begin by proposing the generalized deformed \mathbb{Z}_3 TC wavefunction. Next, we demonstrate that the norm of the wavefunction maps to a previously unreported classical model that extends the Ashkin-Teller (AT) model, which we term the AT_3 model. Finally, we analyze the phase diagram by employing the VUMPS method to evaluate the norm of the wavefunction in the thermodynamic limit.

5.1 Generalized Deformed \mathbb{Z}_3 TC

We start by defining the generalized deformed \mathbb{Z}_3 TC wavefunction as follows:

$$|\tilde{\Psi}(\beta_x, \beta_z)\rangle = \prod_l D_l(\beta_x, \beta_z) |\text{TC}_3\rangle, \quad (51)$$

where the deformation operator is given by

$$D_l(\beta_x, \beta_z) \equiv I_l + \tanh\left(\frac{\beta_x}{2}\right)\Gamma_l^x + \tanh\left(\frac{\beta_z}{2}\right)\Gamma_l^z. \quad (52)$$

This deformation transforms the local basis states $|0\rangle$, $|1\rangle$, and $|2\rangle$ as:

$$\begin{aligned} |0\rangle &\xrightarrow{D(\beta_x, \beta_z)} |\tilde{0}\rangle \propto \left(1 - \frac{1}{3}t_x + t_z\right)|0\rangle + \frac{2}{3}t_x(|1\rangle + |2\rangle), \\ |1\rangle &\xrightarrow{D(\beta_x, \beta_z)} |\tilde{1}\rangle \propto \left(1 - \frac{1}{3}t_x - t_z\right)|1\rangle + \frac{2}{3}t_x(|0\rangle + |2\rangle), \\ |2\rangle &\xrightarrow{D(\beta_x, \beta_z)} |\tilde{2}\rangle \propto \left(1 - \frac{1}{3}t_x - t_z\right)|2\rangle + \frac{2}{3}t_x(|0\rangle + |1\rangle). \end{aligned} \quad (53)$$

Here, we introduce two variational parameters, $(t_x, t_z) \equiv \left(\tanh\frac{\beta_x}{2}, \tanh\frac{\beta_z}{2}\right)$, to simplify the expressions.

Normalizing $\langle \tilde{0} | \tilde{0} \rangle = 1$, the overlaps of local basis are given by

$$\begin{aligned} \langle \tilde{1} | \tilde{1} \rangle = \langle \tilde{2} | \tilde{2} \rangle &= \frac{8t_x^2 + (3t_z + t_x - 3)^2}{8t_x^2 + (3t_z - t_x + 3)^2} \equiv \nu, \\ \langle \tilde{0} | \tilde{1} \rangle = \langle \tilde{0} | \tilde{2} \rangle &= \frac{12t_x}{8t_x^2 + (3t_z - t_x + 3)^2} \equiv \mu, \\ \langle \tilde{1} | \tilde{2} \rangle &= \frac{12t_x(1 - t_z)}{8t_x^2 + (3t_z - t_x + 3)^2} \equiv \rho. \end{aligned} \quad (54)$$

Previously, we have shown that Γ^x and Γ^z transform as $\Gamma^x \leftrightarrow \Gamma^z$ under the duality \mathcal{D}_{e-m} defined in Eq. (4). As a result, the deformed \mathbb{Z}_3 toric code exhibits a $t_x \leftrightarrow t_z$ duality, such that $|\tilde{\Psi}(t_x, t_z)\rangle$ maps to $|\tilde{\Psi}(t_z, t_x)\rangle$. Consequently, the phase diagram of the deformed wavefunction is symmetric about the $t_z = t_x$ line, as shown in Fig. 10.

We note that, unlike the \mathbb{Z}_2 case (reviewed in Appendix A), the deformed \mathbb{Z}_3 toric code does not possess a sign-change duality. In the \mathbb{Z}_2 case, the anti-commutation relation $\{X, Z\} = 0$ implies that $|\psi(h_x, h_z)\rangle$ and $|\psi(-h_x, h_z)\rangle$ are related by a unitary transformation, making the phase diagram symmetric about the $h_x = 0$ and $h_z = 0$ axes. Since no such anti-commutation relation exists for the \mathbb{Z}_3 generalized Pauli matrices, this additional symmetry is absent, leading to a richer phase structure even in the single-parameter deformation regime.

5.2 Mapping to Classical Ashkin-Teller Like Model

The phase diagram of the generalized deformed \mathbb{Z}_3 toric code (TC) can be analyzed by examining the norm of the wavefunction:

$$\langle \tilde{\Psi}(t_x, t_z) | \tilde{\Psi}(t_x, t_z) \rangle = \sum_{c_i, c_j} \langle \tilde{c}_i | \tilde{c}_j \rangle = \sum_{c_i, c_j} [\nu]^{l_{c_i \parallel c_j}} [\rho]^{l_{c_i \nabla c_j}} [\mu]^{l_{c_i} + l_{c_j} - l_{c_i \parallel c_j} - l_{c_i \nabla c_j}}. \quad (55)$$

Here, $|\tilde{c}_i\rangle = D_l(t_x, t_z)|c_i\rangle$ represents closed-loop configurations with the deformation $D_l(t_x, t_z)$ applied. The term l_{c_i} denotes the total loop length in the configuration c_i , $l_{c_i \parallel c_j}$ represents the length of overlapping loops aligned in the same direction between c_i and c_j , and $l_{c_i \nabla c_j}$ represents the length of overlapping loops aligned in opposite directions between c_i and c_j . The summation over these overlap configurations is depicted in Fig. 9. In this figure, blue lines indicate links where loops from c_i and c_j overlap with parallel alignment, contributing a total length of $l_{c_i \parallel c_j}$. Magenta lines indicate links where loops from c_i and c_j overlap with anti-parallel alignment, contributing a total length of $l_{c_i \nabla c_j}$. Green lines represent links occupied

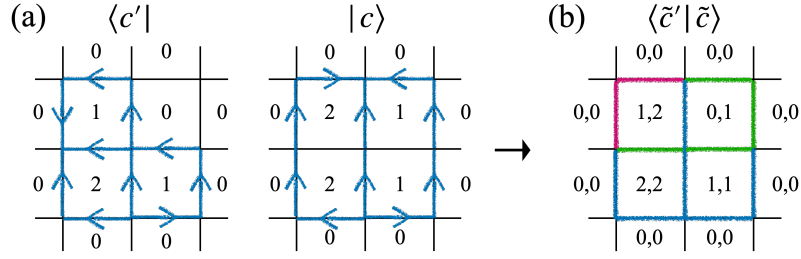


Figure 9: Illustration of the overlap $\langle \tilde{c}' | \tilde{c} \rangle$ between two closed-loop configurations. (a) Two example configurations $\langle c' |$ (left) and $| c \rangle$ (right) on the honeycomb lattice, where the arrows indicate the \mathbb{Z}_3 loop orientation and each plaquette is labeled by its \mathbb{Z}_3 charge. (b) The resulting overlap $\langle \tilde{c}' | \tilde{c} \rangle$, where each plaquette carries a pair of numbers from the bra and ket configurations. Blue lines mark links where loops from c' and c overlap with parallel alignment, contributing to $l_{c' \parallel c}$. Magenta lines mark links where loops overlap with anti-parallel alignment, contributing to $l_{c' \nabla c}$. Green lines mark links occupied by a loop from only one of the two configurations.

by a loop from either c_i or c_j but not both, contributing a total length of $l_{c_i} + l_{c_j} - l_{c_i \parallel c_j} - l_{c_i \nabla c_j}$. Each plaquette contains two numbers: one from the ket configuration and the other from the bra configuration of the closed loop.

From the previous discussion, it follows that the confinement of e anyons is associated with the suppression of blue lines, which correspond to the local overlap $\nu = \langle \tilde{1} | \tilde{1} \rangle = \langle \tilde{2} | \tilde{2} \rangle$. In contrast, the condensation of e anyons is linked to the proliferation of magenta or green lines, which correspond to the local discrepancy overlaps $\mu = \langle \tilde{0} | \tilde{1} \rangle = \langle \tilde{0} | \tilde{2} \rangle$ or $\rho = \langle \tilde{1} | \tilde{2} \rangle$.

One can get further insights by mapping the norm of deformed wavefunction in Eq. (55) into the classical partition function of which Hamiltonian is defined as following

$$H_{\text{AT}_3} = -J_2 \sum_{\langle i,j \rangle} (\delta_{s_i, s_j} + \delta_{\sigma_i, \sigma_j}) - J_{4,1} \sum_{\langle i,j \rangle} (\delta_{s_i - \sigma_i, s_j - \sigma_j}) - J_{4,2} \sum_{\langle i,j \rangle} (\delta_{s_i + \sigma_i, \sigma_j + s_j}). \quad (56)$$

This model, referred to as AT_3 , serves as the \mathbb{Z}_3 generalization of Ashkin-Teller model. Each site i is defined by two \mathbb{Z}_3 spins s_i and σ_i .

By associating (s_i, σ_i) with pairs of \mathbb{Z}_3 numbers, Fig. 9 also represents classical configurations of the AT_3 model. In this classical model, local excitations depend on the differences between neighboring site variables. These excitations correspond to the three types of colored lines observed in the overlap of loop configurations $\langle \tilde{c}_i | \tilde{c}_j \rangle$ [Fig. 9(b)], with their Boltzmann weights mapping onto the quantum system as follows:

$$\begin{aligned} \text{(Blue line)} & \quad \exp(-2\beta_2 - \beta_{4,2}) = \nu, \\ \text{(Magenta line)} & \quad \exp(-2\beta_2 - \beta_{4,1}) = \mu, \\ \text{(Green line)} & \quad \exp(-\beta_2 - \beta_{4,1} - \beta_{4,2}) = \rho. \end{aligned} \quad (57)$$

Here, $\beta_2 = J_2/T$, $\beta_{4,1} = J_{4,1}/T$, and $\beta_{4,2} = J_{4,2}/T$, where T represents temperature. Using the mapping defined in Eq. (57), the classical partition function can be related to the norm of the deformed \mathbb{Z}_3 TC wavefunction as $Z_{\text{AT}_3} = \langle \tilde{\Psi}(\beta_x, \beta_z) | \tilde{\Psi}(\beta_x, \beta_z) \rangle$.

The AT_3 model possesses two evident global symmetries, defined as:

$$U_1 = \prod_i X_i^s, \quad \text{and} \quad U_2 = \prod_i X_i^s X_i^\sigma, \quad (58)$$

where X_i^s and X_i^σ cyclically rotate the local \mathbb{Z}_3 variables s_i and σ_i , respectively. The order parameters corresponding to the spontaneous breaking of each symmetry are given by:

$$\langle \omega^{s_i} \omega^{\sigma_i} \rangle, \quad \text{and} \quad \langle \omega^{\sigma_i} \rangle. \quad (59)$$

Here, $\omega = \exp(2\pi i/3)$.

The order parameter $\langle \omega^{s_i} \omega^{\sigma_i} \rangle$ characterizes the ordering of the two \mathbb{Z}_3 numbers. When these two \mathbb{Z}_3 numbers are ordered, the discrepancy lines represented by μ and ρ are suppressed, indicating that the e anyons remain uncondensed in this phase.

Conversely, the order parameter $\langle \omega^{\sigma_i} \rangle$ reflects the ordering of the \mathbb{Z}_3 number σ_i . Due to the symmetry of the model under the exchange of s_i and σ_i , the ordering of σ_i implies the ordering of s_i as well. Furthermore, as confirmed through numerical analysis and shown in Fig. 10, the order parameter $\langle \omega^{\sigma_i} \rangle$ or $\langle \omega^{s_i} \rangle$ can have a finite value only when $\langle \omega^{s_i} \omega^{\sigma_i} \rangle \neq 0$. This indicates that the discrepancy lines are suppressed in the net configuration when either s_i or σ_i is ordered. In this scenario, the configuration contains only the blue nets represented by ν . When $\langle \sigma_i \rangle \neq 0$, the blue lines are further suppressed, signifying that the e anyons are confined.

5.3 PEPS Representation and Injective Symmetries

The tensor network framework establishes a connection between the classical order parameters and the condensation or confinement of e anyons in the deformed \mathbb{Z}_3 TC. We begin by introducing the PEPS representation for the \mathbb{Z}_3 TC:

$$|\text{TC}_3\rangle = \begin{array}{c} \begin{array}{cccc} \bullet & \bullet & \bullet & \bullet \\ \bullet & \bullet & \bullet & \bullet \\ \bullet & \bullet & \bullet & \bullet \\ \bullet & \bullet & \bullet & \bullet \end{array} \\ \text{(Diagram showing a 4x4 grid of nodes with solid lines forming a rotated square lattice and dashed lines forming a grid)} \end{array} \quad (60)$$

In this representation, the solid lines denote the square lattice shown in Fig. 1, which is obtained by rotating the original square lattice 45° counterclockwise. The PEPS representation is constructed by contracting the virtual indices of the local PEPS tensor defined as:

$$\mathbb{A}_{s_u s_d s_l s_r}^{m_1 m_2 m_3 m_4} = \begin{array}{c} \begin{array}{ccc} & s_u & \\ m_2 & \bullet & m_1 \\ & \bullet & \\ s_l & \bullet & s_r \\ & \bullet & \\ & s_d & \\ m_3 & \bullet & m_4 \end{array} \end{array} \quad (61)$$

The local tensor, $\mathbb{A}_{s_u s_d s_l s_r}^{m_1 m_2 m_3 m_4}$, includes virtual indices s_u, s_d, s_l , and s_r , and physical indices m_1, m_2, m_3 , and m_4 . The virtual indices are internal degrees of freedom used for tensor contractions, while the physical indices represent local \mathbb{Z}_3 spins. Each index takes values 0, 1, 2. The tensor element $\mathbb{A}_{s_u s_d s_l s_r}^{m_1 m_2 m_3 m_4} = 1$ if the following conditions are satisfied:

$$\begin{aligned} m_1 &= s_u - s_r \pmod{3}, & m_2 &= -s_u + s_l \pmod{3}, \\ m_3 &= -s_d + s_l \pmod{3}, & m_4 &= s_d - s_r \pmod{3}. \end{aligned} \quad (62)$$

Otherwise, $\mathbb{A}_{s_u s_d s_l s_r}^{m_1 m_2 m_3 m_4} = 0$.

The tensor \mathbb{A} is designed to generate the closed-loop configurations of the \mathbb{Z}_3 TC. The values of the virtual bonds correspond to the numbers on the plaquette crossed by the bond, indicating the number of times the b_p operator is applied to the plaquette. The physical bonds in Eq. (62) are assigned to represent the domain walls between neighboring plaquettes.

Operations on the physical indices of the tensor $\mathbb{A}_{s_u s_d s_l s_r}^{m_1 m_2 m_3 m_4}$ can be expressed in terms of corresponding operations on the virtual indices:

Diagrammatic equations (63) showing operations on the tensor \mathbb{A} with X and X^{-1} on physical indices and virtual indices. The equations are arranged in two rows and two columns, showing how operations on physical indices translate to operations on virtual indices.

and

Diagrammatic equations (64) showing operations on the tensor \mathbb{A} with Z and Z^{-1} on physical indices and virtual indices. The equations are arranged in two rows and two columns, showing how operations on physical indices translate to operations on virtual indices.

In particular, Eq. (63) defines the \mathbb{Z}_3 -injective symmetry of the local tensor as:

$$\mathbb{A}_{s_u s_d s_l s_r}^{m_1 m_2 m_3 m_4}(u_g \otimes u_g \otimes u_g^\dagger \otimes u_g^\dagger) = \mathbb{A}_{s_u s_d s_l s_r}^{m_1 m_2 m_3 m_4}$$

Diagrammatic equation (65) showing the \mathbb{Z}_3 -injective symmetry of the local tensor. The left side shows the tensor with X and X^{-1} on physical indices, and the right side shows the tensor with X and X^{-1} on virtual indices.

where $u_g \in \{I, X, X^2\}$.

The PEPS representation for the deformed \mathbb{Z}_3 TC is obtained by contracting the deformed local tensor, defined as:

$$\mathbb{A}_{s_u s_d s_l s_r}^{m_1 m_2 m_3 m_4} = \mathbb{A}_{s_u s_d s_l s_r}^{m_1 m_2 m_3 m_4} D_{s_1}(\beta_x, \beta_z) D_{s_2}(\beta_x, \beta_z) D_{s_3}(\beta_x, \beta_z) D_{s_4}(\beta_x, \beta_z).$$

Since the deformations are applied exclusively to the physical indices while leaving the virtual indices unchanged, the deformed tensor retains the same injective symmetry as described in Eq. (65).

Using the PEPS representation, the overlap of the deformed wavefunction can be expressed as:

$$\langle \Psi(\beta_x, \beta_z) | \Psi(\beta_x, \beta_z) \rangle = \text{Tr}(\mathbb{T}_\Psi)^{L_x} = (\mathbb{T}_\Psi)^{L_x}$$

Diagrammatic representation of the wavefunction overlap as a trace of a transfer matrix. The left side shows a grid of tensors with physical indices contracted, and the right side shows the trace of the transfer matrix \mathbb{T}_Ψ raised to the power L_x .

5.4 Phase diagram

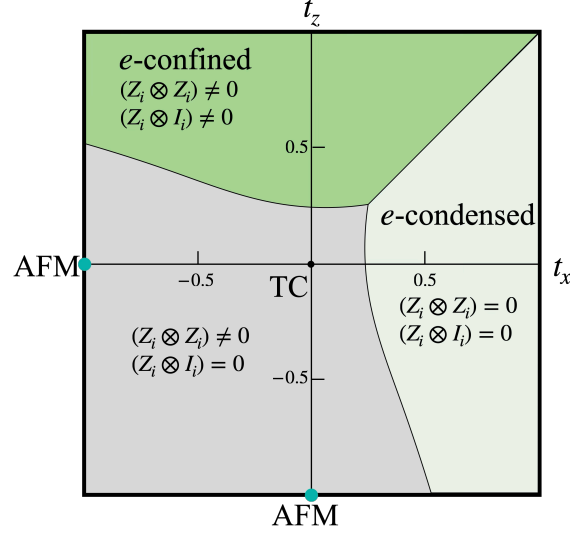


Figure 10: Phase diagram of the deformed \mathbb{Z}_3 toric code as a function of the variational parameters $t_x = \tanh(\beta_x/2)$ and $t_z = \tanh(\beta_z/2)$, obtained from VUMPS analysis. Three phases are identified: the TC phase (gray, $(Z_i \otimes Z_i) \neq 0$, $(Z_i \otimes I_i) = 0$), the e -confined phase (dark green, both order parameters nonzero), and the e -condensed phase (light green, both order parameters zero). The phase diagram is symmetric about the $t_z = t_x$ line due to the \mathcal{D}_{e-m} duality. Two isolated AFM critical points (cyan dots) with $c = 1$ are located at $(t_x, t_z) = (-1, 0)$ and $(0, -1)$.

Recall that the norm of the deformed \mathbb{Z}_3 TC ($\langle \tilde{\Psi}(\beta_x, \beta_z) | \tilde{\Psi}(\beta_x, \beta_z) \rangle$) or the classical partition function of the AT_3 model (Z_{AT_3}) can be expressed as a repeated product of the column-to-column transfer matrix \mathbb{T}_Ψ or \mathbb{T}_{AT_3} , respectively. This involves applying the transfer matrix \mathbb{T} L_x times to the far-right boundary state $|\varphi_r^0\rangle$ and taking the overlap with the far-left boundary state $\langle \varphi_l^0|$. Specifically, these quantities can be written as:

$$\langle \tilde{\Psi}(\beta_x, \beta_z) | \tilde{\Psi}(\beta_x, \beta_z) \rangle = \langle \varphi_l^0 | [\mathbb{T}_\Psi]^{L_x} | \varphi_r^0 \rangle, \quad (72)$$

$$Z_{\text{AT}_3} = \langle \varphi_l^0 | [\mathbb{T}_{\text{AT}_3}]^{L_x} | \varphi_r^0 \rangle. \quad (73)$$

Now, consider a right boundary state evolved by applying the transfer matrix x times: $|\varphi_r^x\rangle = [\mathbb{T}]^x |\varphi_r^0\rangle$. In the thermodynamic limit, this state satisfies the relation $|\varphi_r^{x+1}\rangle = \mathbb{T}|\varphi_r^x\rangle \propto |\varphi_r^x\rangle$. This implies that the right boundary state $|\varphi_r^x\rangle$ in the thermodynamic limit corresponds to the eigenstate of the transfer matrix \mathbb{T} associated with the largest eigenvalue. Eigenstates with smaller eigenvalues vanish under repeated applications of \mathbb{T} due to normalization effects.

Using the VUMPS method [16], we numerically compute the fixed-point eigenstate of the transfer matrix \mathbb{T} . In Ref. [17], it is demonstrated that the spontaneous symmetry breaking of the two global symmetries of the transfer matrix, \mathcal{U}_1 and \mathcal{U}_2 , is directly connected to the confinement and condensation of e anyons. The phase diagram of the deformed toric code, derived from the analysis of the order parameters $(Z_i \otimes I_i)$ and $(Z_i \otimes Z_i)$, is shown in Fig. 10, where the x - and y -axes represent the deformation parameters t_x and t_z , respectively.

The TC point lies in a phase characterized by $(Z_i \otimes Z_i) \neq 0$ and $(Z_i \otimes I_i) = 0$. Here, $(Z_i \otimes Z_i) \neq 0$ indicates that the e anyons are not condensed, while $(Z_i \otimes I_i) = 0$ indicates that the e anyons are deconfined. As t_x increases, the system transitions to a fully symmetric phase, where $(Z_i \otimes Z_i) = 0$, indicating that the e anyons are condensed. Conversely, as t_z increases,

the system transitions to a fully symmetry-broken phase, where $(Z_i \otimes I_i) \neq 0$, signifying that the e anyons are confined.

In the context of the classical AT_3 model, the spontaneous symmetry breaking of the fixed point $|\varphi_r^x\rangle$ corresponds directly to the symmetry breaking of the global symmetries of the AT_3 system. The TC phase, the e -confined phase, and the e -condensed phase correspond to the partially ordered phase, the fully ordered FM phase, and the paramagnetic phase of the classical AT_3 model, respectively. These phases are also present in the \mathbb{Z}_2 version of the original Ashkin-Teller model.

However, the critical points at $(t_x, t_z) = (-1, 0)$ and $(t_x, t_z) = (0, -1)$, corresponding to the AFM critical point of the $Q = 3$ Potts model, represent novel features absent in the original Ashkin-Teller model. Since the AT_3 model includes three variational parameters while the presented phase diagram accounts for only two, it has the potential to host a richer variety of phases, necessitating further investigation in future study.

5.5 Criticalities

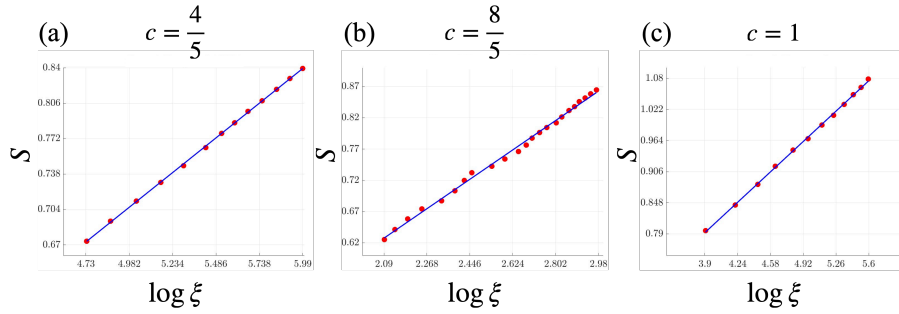


Figure 11: Central charge determination at the critical points from the Calabrese–Cardy scaling of entanglement entropy S versus the logarithm of the correlation length $\log \xi$ of the VUMPS fixed-point state. (a) The phase boundary between the TC and e -condensed (or e -confined) phases yields $c = 4/5$, corresponding to the \mathbb{Z}_3 parafermion CFT. (b) The merged critical line separating the e -confined and e -condensed phases gives $c = 8/5$. (c) The isolated AFM critical points exhibit $c = 1$, consistent with the \mathbb{Z}_4 parafermion CFT.

We analyzed the central charges at the critical points by fitting the entanglement entropy and correlation length of the fixed point $|\varphi_r^x\rangle$ to the Calabrese-Cardy formula, as illustrated in Fig. 11. The phase boundaries between the TC phase and the e -condensed or e -confined phases contain critical points described by the $Q = 3$ Potts model, which corresponds to a \mathbb{Z}_3 parafermion CFT. The central charge $c = \frac{4}{5}$ at these critical points is confirmed, as shown in Fig. 11(a).

The two phase boundaries merge into a single critical line dividing the e -confined and e -condensed phases. Along this line, the central charge is $c = \frac{8}{5}$, as depicted in Fig. 11(b). Lastly, two isolated antiferromagnetic (AFM) critical points are identified within the e -confined and e -condensed phases, respectively. These points exhibit a central charge of $c = 1$, consistent with the \mathbb{Z}_4 parafermion CFT, as depicted in Fig. 11(c).

6 Conclusion

In this work, we have systematically investigated the deformed \mathbb{Z}_3 toric code and its topological phase transitions. Starting from the \mathbb{Z}_3 cluster state defined on the Lieb lattice, we

demonstrated that a deformed \mathbb{Z}_3 toric code state can be generated through a measurement-based protocol analogous to the \mathbb{Z}_2 case, where the deformation is controlled by rotating the local qutrit basis prior to measurement. We showed that this deformed state is equivalently obtained by applying a filtering operator $D_l(\beta_x)$ or its dual $D_l(\beta_z)$ to the \mathbb{Z}_3 toric code ground state, and derived the corresponding parent Hamiltonian.

Using the loop-gas and net configuration framework, we analyzed the phase diagrams for the single-parameter deformations β_z and β_x separately. In the β_z direction, we mapped the wavefunction norm to the partition function of the $Q = 3$ Potts model, identifying a phase transition from the topologically ordered (TC) phase to an e -confined phase at the FM critical point $\exp(\beta_c) = 1 + \sqrt{3}$, governed by a \mathbb{Z}_3 parafermion CFT with central charge $c = 4/5$. In the β_x direction, the dual analysis reveals a transition to an e -condensed phase at the corresponding critical point. At the extreme deformation limit $\beta_z \rightarrow -\infty$ (or equivalently $\beta_x \rightarrow -\infty$ under duality), the system reduces to the square ice model with an emergent $U(1)$ 1-form symmetry, leading to Hilbert space fragmentation and an exponentially growing number of scar states.

For the general two-parameter deformation, we introduced the generalized deformed \mathbb{Z}_3 toric code wavefunction $|\tilde{\Psi}(\beta_x, \beta_z)\rangle$ and showed that its norm maps to the partition function of a previously unreported classical model—the AT_3 model—which serves as the \mathbb{Z}_3 generalization of the Ashkin-Teller model. The AT_3 model possesses two independent \mathbb{Z}_3 global symmetries whose spontaneous breaking patterns correspond to the condensation and confinement of e anyons. Using the PEPS representation and the VUMPS method, we numerically determined the full phase diagram in the (t_x, t_z) parameter space, identifying three distinct phases: the TC phase, the e -confined phase, and the e -condensed phase. The phase boundaries host critical points with central charges $c = 4/5$, $c = 8/5$ (at the merged boundary), and $c = 1$ (at the isolated AFM critical points), respectively.

A notable distinction from the \mathbb{Z}_2 case is the absence of the sign-change duality, which arises from the anti-commutation relation $\{X, Z\} = 0$ specific to qubits. This leads to a richer and less symmetric phase structure in the \mathbb{Z}_3 case. Furthermore, the AT_3 model, which involves three independent coupling constants, has the potential to host additional phases beyond the two-parameter subspace explored here.

Several directions remain for future investigation. First, the AT_3 model warrants a more comprehensive study in its full three-parameter space, which may reveal phases absent in the standard Ashkin-Teller model. Second, the emergent $U(1)$ symmetry at the square ice point and its connection to Hilbert space fragmentation deserve further exploration, particularly in the context of non-ergodic dynamics and quantum many-body scars. Third, extending the present framework to other \mathbb{Z}_N generalizations or to non-Abelian topological codes may yield additional insights into the interplay between measurement-based quantum computation and topological order. Finally, studying the entanglement structure and the minimally entangled states of the deformed wavefunction across the full phase diagram could provide a deeper understanding of the topological-to-trivial transitions.

Acknowledgements

Funding information This work was supported by the Basic Science Research Program through the National Research Foundation of Korea funded by the Ministry of Science and ICT [Grant No. RS-2023-00220471, RS-2025-16064392].

A Review: Deformed \mathbb{Z}_2 Toric Code

In this appendix, we review the approach presented in Ref. [11], where the phase diagram of the deformed \mathbb{Z}_2 toric code wavefunction is derived by mapping its norm to the partition functions of classical models. In certain limits of the deformation parameters, the norm of the deformed wavefunction maps directly to the partition function of the classical Ising model. The condensation and confinement of electric (e) anyons are closely tied to the symmetry-breaking transitions of the corresponding classical Ising model. In the more general parameter regime, the norm of the wavefunction maps to the partition function of the Ashkin-Teller (AT) model [18–21]. The phases of the Ising model generalize into three distinct phases of the AT model, which are characterized by two order parameters. These three phases correspond to the three phases of the deformed \mathbb{Z}_2 toric code wavefunction, as illustrated in Fig. 12.

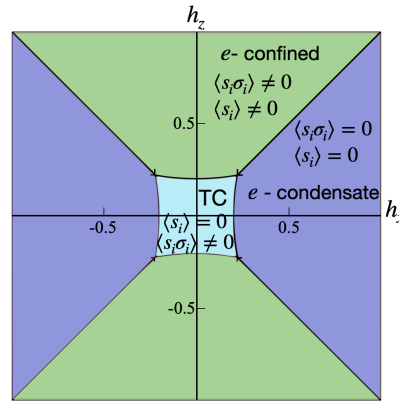


Figure 12: The phase diagram of the deformed \mathbb{Z}_2 toric code as a function of the variational parameters h_x and h_z . The order parameters of the corresponding classical AT phases, $\langle s_i \rangle$ and $\langle s_i \sigma_i \rangle$, are indicated.

A.1 Loop-gas picture

$$|\psi\rangle = |c_0\rangle + |c_1\rangle + \dots + |c_i\rangle + |c_j\rangle + \dots$$

Figure 13: (a) Examples of the \mathbb{Z}_2 loop-gas configurations appearing in the overlap of the deformed \mathbb{Z}_2 TC for the h_z deformation. Orange loops represent the overlap $\langle \tilde{1} | \tilde{1} \rangle = \nu$. (b) Overlap configurations for the h_x deformation, where green loops correspond to the discrepancy overlap $\langle \tilde{0} | \tilde{1} \rangle = \mu$ and orange loops to $\langle \tilde{1} | \tilde{1} \rangle = \nu$.

We analyze the phases of the deformed toric code by examining the wavefunction norm through its mapping to a classical model. Each term in the expansion of Eq. (8) corresponds to a closed-loop configuration, as illustrated in Fig. 13(a). The number at the center of a plaquette indicates whether the stabilizer b_p is applied (-1) or not (1). The loops act as domain walls separating regions labeled by 1 and -1 , and these loops are always closed. On the links, an occupied link represents the local state $|1\rangle$, while an empty link corresponds to $|0\rangle$.

The bare ground state wavefunction, without deformation, is an equal superposition of all

possible closed-loop configurations:

$$|\text{TC}_2\rangle = \sum_c |c\rangle, \quad (\text{A.1})$$

where the summation runs over all possible closed-loop configurations c , which form an orthonormal basis.

In the loop-gas representation, the loops are closely tied to e anyons. Each anyon corresponds to the endpoint of a loop, where $a_v = -1$. In the ground state, only closed-loop configurations are present, ensuring $a_v = 1$ at every vertex. Anyons are created in pairs by “cutting” a loop, introducing open loops with e anyons at the endpoints.

A.2 Wavefunction deformation

The deformed \mathbb{Z}_2 toric code wavefunction is expressed as:

$$|\psi(h_x, h_z)\rangle = P_2(h_x, h_z)|\text{TC}_2\rangle = \sum_c |\tilde{c}\rangle, \quad (\text{A.2})$$

where the deformation operator $P_2(h_x, h_z) \equiv \prod_l p_{2,l}(h_x, h_z)$ with

$$p_{2,l}(h_x, h_z) = \mathbb{I}_{2,l} + h_x X_l + h_z Z_l. \quad (\text{A.3})$$

Here, X and Z are \mathbb{Z}_2 Pauli operators. The deformation operator rotates and adjusts the norm of the local states:

$$|0\rangle \rightarrow |\tilde{0}\rangle = \begin{pmatrix} 1 + h_z \\ h_x \end{pmatrix}, \quad |1\rangle \rightarrow |\tilde{1}\rangle = \begin{pmatrix} h_x \\ 1 - h_z \end{pmatrix}. \quad (\text{A.4})$$

Setting $\langle \tilde{0} | \tilde{0} \rangle = 1$, the overlaps between local states are:

$$\langle \tilde{1} | \tilde{1} \rangle = \frac{h_x^2 + (h_z - 1)^2}{h_x^2 + (h_z + 1)^2} \equiv \nu, \quad \langle \tilde{1} | \tilde{0} \rangle = \frac{2h_x}{h_x^2 + (h_z + 1)^2} \equiv \mu. \quad (\text{A.5})$$

The deformed wavefunction transforms as $|\psi(h_x, h_z)\rangle \leftrightarrow |\psi(h_z, h_x)\rangle$ under the dual transformation \mathcal{D}_{e-m} . Furthermore, in the \mathbb{Z}_2 case, there exists an additional sign-change duality arising from the anti-commutation relation $\{X, Z\} = 0$. Applying $\prod_l Z_l$ to the deformed wavefunction yields:

$$\prod_l Z_l |\psi(h_x, h_z)\rangle = P_2(-h_x, h_z) \prod_l Z_l |\text{TC}_2\rangle = |\psi(-h_x, h_z)\rangle. \quad (\text{A.6})$$

Similarly, applying $\prod_l X_l$ establishes the $h_z \leftrightarrow -h_z$ duality. Consequently, the phase diagram is symmetric about the $h_z = h_x$, $h_x = 0$, and $h_z = 0$ axes, as shown in Fig. 12.

A.3 Mapping to classical Ising model

We begin by examining the limits $h_x = 0$ and $h_z = 0$. When $h_x = 0$, the deformed local states reduce to $|\tilde{0}\rangle = |0\rangle$ and $|\tilde{1}\rangle = \sqrt{\nu}|1\rangle$. The norm of the deformed wavefunction becomes:

$$\langle \psi(0, h_z) | \psi(0, h_z) \rangle = \sum_c \nu^{l_c}, \quad (\text{A.7})$$

where l_c is the total length of loops in configuration c . This is illustrated in Fig. 14(a), where the orange loops represent the overlap $\langle \tilde{1} | \tilde{1} \rangle = \nu$.

(a) $\langle \tilde{c}_0 | \tilde{c}_0 \rangle = 1$ $\langle \tilde{c}_1 | \tilde{c}_1 \rangle = \nu^{l_{c_1}}$ $\langle \tilde{c}_i | \tilde{c}_i \rangle = \nu^{l_{c_i}}$ $\langle \tilde{c}_j | \tilde{c}_j \rangle = \nu^{l_{c_j}}$

$$\langle \psi(0, h_z) | \psi(0, h_z) \rangle = \begin{array}{ccccccc} \begin{array}{|c|c|c|c|} \hline 1,1 & 1,1 & & \\ \hline 1,1 & 1,1 & 1,1 & 1,1 \\ \hline 1,1 & 1,1 & 1,1 & 1,1 \\ \hline 1,1 & 1,1 & & \\ \hline \end{array} & + & \begin{array}{|c|c|c|c|} \hline 1,1 & 1,1 & & \\ \hline 1,1 & 1,1 & 1,1 & 1,1 \\ \hline 1,1 & -1,-1 & 1,1 & 1,1 \\ \hline 1,1 & 1,1 & & \\ \hline \end{array} & \cdots + & \begin{array}{|c|c|c|c|} \hline 1,1 & 1,1 & & \\ \hline 1,1 & 1,1 & -1,-1 & 1,1 \\ \hline 1,1 & -1,-1 & -1,-1 & 1,1 \\ \hline 1,1 & 1,1 & & \\ \hline \end{array} & + & \begin{array}{|c|c|c|c|} \hline 1,1 & 1,1 & & \\ \hline 1,1 & 1,1 & -1,-1 & 1,1 \\ \hline 1,1 & 1,1 & -1,-1 & 1,1 \\ \hline 1,1 & 1,1 & & \\ \hline \end{array} & + & \cdots \end{array}$$

(b) $\langle \tilde{c}_0 | \tilde{c}_0 \rangle = 1$ $\langle \tilde{c}_1 | \tilde{c}_1 \rangle = \mu^{l_{c_1}}$ $\langle \tilde{c}_0 | \tilde{c}_i \rangle = \mu^{l_{c_i}}$ $\langle \tilde{c}_0 | \tilde{c}_j \rangle = \mu^{l_{c_j}}$

$$\langle \psi(h_x, 0) | \psi(h_x, 0) \rangle = \begin{array}{ccccccc} \begin{array}{|c|c|c|c|} \hline 1,1 & 1,1 & & \\ \hline 1,1 & 1,1 & 1,1 & 1,1 \\ \hline 1,1 & 1,1 & 1,1 & 1,1 \\ \hline 1,1 & 1,1 & & \\ \hline \end{array} & + & \begin{array}{|c|c|c|c|} \hline 1,1 & 1,1 & & \\ \hline 1,1 & 1,1 & 1,1 & 1,1 \\ \hline 1,1 & -1,-1 & 1,1 & 1,1 \\ \hline 1,1 & 1,1 & & \\ \hline \end{array} & \cdots + & \begin{array}{|c|c|c|c|} \hline 1,1 & 1,1 & & \\ \hline 1,1 & 1,1 & 1,-1 & 1,1 \\ \hline 1,1 & -1,-1 & 1,-1 & 1,1 \\ \hline 1,1 & 1,1 & & \\ \hline \end{array} & + & \begin{array}{|c|c|c|c|} \hline 1,1 & 1,1 & & \\ \hline 1,1 & 1,1 & 1,-1 & 1,1 \\ \hline 1,1 & 1,1 & 1,-1 & 1,1 \\ \hline 1,1 & 1,1 & & \\ \hline \end{array} & + & \cdots \end{array}$$

+ $\begin{array}{ccccccc} \begin{array}{|c|c|c|c|} \hline 1,1 & 1,1 & & \\ \hline 1,1 & 1,1 & 1,1 & 1,1 \\ \hline 1,1 & -1,-1 & 1,1 & 1,1 \\ \hline 1,1 & 1,1 & & \\ \hline \end{array} & + & \begin{array}{|c|c|c|c|} \hline 1,1 & 1,1 & & \\ \hline 1,1 & 1,1 & 1,1 & 1,1 \\ \hline 1,1 & -1,-1 & 1,1 & 1,1 \\ \hline 1,1 & 1,1 & & \\ \hline \end{array} & \cdots + & \begin{array}{|c|c|c|c|} \hline 1,1 & 1,1 & & \\ \hline 1,1 & 1,1 & 1,-1 & 1,1 \\ \hline 1,1 & -1,-1 & 1,-1 & 1,1 \\ \hline 1,1 & 1,1 & & \\ \hline \end{array} & + & \begin{array}{|c|c|c|c|} \hline 1,1 & 1,1 & & \\ \hline 1,1 & 1,1 & 1,-1 & 1,1 \\ \hline 1,1 & -1,-1 & 1,-1 & 1,1 \\ \hline 1,1 & 1,1 & & \\ \hline \end{array} & + & \cdots \end{array}$

$\langle \tilde{c}_1 | \tilde{c}_i \rangle = \mu^{l_{c_0} + l_{c_j} - l_{c_0 c_j}}$ $\langle \tilde{c}_1 | \tilde{c}_i \rangle = \mu^{l_{c_0} + l_{c_i} - l_{c_0 c_i}}$

Figure 14: (a) Overlap configurations for the h_z deformation ($h_x = 0$), where each configuration contributes a weight ν^{l_c} . The orange loops represent domain walls of the classical Ising model. (b) Overlap configurations for the h_x deformation ($h_z = 0$), involving both orange and green loops. Green loops represent domain walls of the product spin $S_i = s_i \sigma_i$.

The norm maps to the partition function of the classical Ising model:

$$H_{\text{Ising}} = -J_1 \sum_{\langle i,j \rangle} s_i s_j, \quad (\text{A.8})$$

with partition function $Z_{\text{Ising}} = \sum_c \exp(-K_1 l_c)$, where $K_1 = J_1/T$. By identifying $\exp(-K_1) = \nu$, we find $\langle \psi(0, h_z) | \psi(0, h_z) \rangle = Z_{\text{Ising}}$. The phase transition occurs at:

$$\nu_c = \frac{1}{1 + \sqrt{2}}. \quad (\text{A.9})$$

For $\nu > \nu_c$, the orange loops proliferate and e anyons are deconfined. For $\nu < \nu_c$, the loops are suppressed and e anyons become confined.

On the other hand, the h_x deformation with $h_z = 0$ leads to the condensation of e anyons. In this case, the norms of the local states remain unchanged, but the orthogonality is broken: $\langle \tilde{0} | \tilde{1} \rangle = \mu \neq 0$. The norm becomes:

$$\langle \psi(h_x, 0) | \psi(h_x, 0) \rangle = \sum_{c, c'} \mu^{l_c + l_{c'} - l_{c c'}} \nu^{l_{c c'}}, \quad (\text{A.10})$$

where c and c' represent two loop-gas configurations, as illustrated in Fig. 14(b). When $h_z = 0$, we have $\nu = 1$, and the norm reduces to:

$$\langle \psi(h_x, 0) | \psi(h_x, 0) \rangle = N_c \sum_{c'} \mu^{l_{c'}}, \quad (\text{A.11})$$

where N_c is the total number of loop configurations. This maps to the partition function of a second Ising model with the product spin $S_i = s_i \sigma_i$:

$$H_{\text{Ising}'} = -J_2 \sum_{\langle i,j \rangle} s_i \sigma_i s_j \sigma_j, \quad (\text{A.12})$$

with a critical point at $\mu_c = 1/(1 + \sqrt{2})$. The green loops, corresponding to domain walls of S_i , drive the condensation of e anyons: for $\mu > \mu_c$, green loops proliferate and e anyons condense; for $\mu < \mu_c$, green loops are suppressed and e anyons remain uncondensed.

A.4 Mapping to Ashkin-Teller model

In the general deformation regime with both h_x and h_z nonzero, both orange and green loops contribute to the norm in Eq. (A.10). In this case, the overlap configurations map to the partition function of the classical Ashkin-Teller (AT) model:

$$H_{\text{AT}} = -J_2 \sum_{\langle i,j \rangle} (s_i s_j + \sigma_i \sigma_j) - J_4 \sum_{\langle i,j \rangle} s_i s_j \sigma_i \sigma_j. \quad (\text{A.13})$$

The AT Hamiltonian combines the two Ising models described above. The three phases of the AT model — the fully ordered phase (both $\langle s_i \rangle \neq 0$ and $\langle s_i \sigma_i \rangle \neq 0$), the partially ordered phase ($\langle s_i \rangle = 0$ but $\langle s_i \sigma_i \rangle \neq 0$), and the disordered phase ($\langle s_i \rangle = 0$ and $\langle s_i \sigma_i \rangle = 0$) — correspond to the e -confined phase, the TC phase, and the e -condensed phase, respectively, as illustrated in Fig. 12. This \mathbb{Z}_2 framework provides the foundation for the \mathbb{Z}_3 generalization discussed in the main text.

References

- [1] R. Raussendorf and H. J. Briegel, *A one-way quantum computer*, Phys. Rev. Lett. **86**, 5188 (2001), doi:[10.1103/PhysRevLett.86.5188](https://doi.org/10.1103/PhysRevLett.86.5188).
- [2] R. Raussendorf, D. E. Browne and H. J. Briegel, *Measurement-based quantum computation on cluster states*, Phys. Rev. A **68**, 022312 (2003), doi:[10.1103/PhysRevA.68.022312](https://doi.org/10.1103/PhysRevA.68.022312).
- [3] M. A. Nielsen, *Cluster-state quantum computation*, Reports on Mathematical Physics **57**(1), 147 (2006), doi:[https://doi.org/10.1016/S0034-4877\(06\)80014-5](https://doi.org/10.1016/S0034-4877(06)80014-5).
- [4] H. J. Briegel, D. E. Browne, W. Dür, R. Raussendorf and M. Van den Nest, *Measurement-based quantum computation*, Nature Physics **5**(1), 19 (2009), doi:[10.1038/nphys1157](https://doi.org/10.1038/nphys1157).
- [5] D. Gross and J. Eisert, *Novel schemes for measurement-based quantum computation*, Phys. Rev. Lett. **98**, 220503 (2007), doi:[10.1103/PhysRevLett.98.220503](https://doi.org/10.1103/PhysRevLett.98.220503).
- [6] M. Van den Nest, A. Miyake, W. Dür and H. J. Briegel, *Universal resources for measurement-based quantum computation*, Phys. Rev. Lett. **97**, 150504 (2006), doi:[10.1103/PhysRevLett.97.150504](https://doi.org/10.1103/PhysRevLett.97.150504).
- [7] R. Raussendorf, S. Bravyi and J. Harrington, *Long-range quantum entanglement in noisy cluster states*, Phys. Rev. A **71**, 062313 (2005), doi:[10.1103/PhysRevA.71.062313](https://doi.org/10.1103/PhysRevA.71.062313).
- [8] B. J. Brown, W. Son, C. V. Kraus, R. Fazio and V. Vedral, *Generating topological order from a two-dimensional cluster state using a duality mapping*, New Journal of Physics **13**(6), 065010 (2011), doi:[10.1088/1367-2630/13/6/065010](https://doi.org/10.1088/1367-2630/13/6/065010).
- [9] A. Kitaev, *Fault-tolerant quantum computation by anyons*, Annals of Physics **303**(1), 2 (2003), doi:[https://doi.org/10.1016/S0003-4916\(02\)00018-0](https://doi.org/10.1016/S0003-4916(02)00018-0).
- [10] R. Raussendorf and J. Harrington, *Fault-tolerant quantum computation with high threshold in two dimensions*, Physical review letters **98**(19), 190504 (2007).

- [11] G.-Y. Zhu and G.-M. Zhang, *Gapless coulomb state emerging from a self-dual topological tensor-network state*, Phys. Rev. Lett. **122**, 176401 (2019), doi:[10.1103/PhysRevLett.122.176401](https://doi.org/10.1103/PhysRevLett.122.176401).
- [12] H. J. Briegel and R. Raussendorf, *Persistent entanglement in arrays of interacting particles*, Phys. Rev. Lett. **86**, 910 (2001), doi:[10.1103/PhysRevLett.86.910](https://doi.org/10.1103/PhysRevLett.86.910).
- [13] J. L. Jacobsen, J.-F. Richard and J. Salas, *Complex-temperature phase diagram of potts and rsos models*, Nuclear Physics B **743**(3), 153 (2006), doi:<https://doi.org/10.1016/j.nuclphysb.2006.02.033>.
- [14] J. L. Jacobsen and H. Saleur, *The antiferromagnetic transition for the square-lattice potts model*, Nuclear Physics B **743**(3), 207 (2006), doi:<https://doi.org/10.1016/j.nuclphysb.2006.02.041>.
- [15] C. Stahl, R. Nandkishore and O. Hart, *Topologically stable ergodicity breaking from emergent higher-form symmetries in generalized quantum loop models*, SciPost Phys. **16**, 068 (2024), doi:[10.21468/SciPostPhys.16.3.068](https://doi.org/10.21468/SciPostPhys.16.3.068).
- [16] M. T. Fishman, L. Vanderstraeten, V. Zauner-Stauber, J. Haegeman and F. Verstraete, *Faster methods for contracting infinite two-dimensional tensor networks*, Phys. Rev. B **98**, 235148 (2018), doi:[10.1103/PhysRevB.98.235148](https://doi.org/10.1103/PhysRevB.98.235148).
- [17] J. Haegeman, V. Zauner, N. Schuch and F. Verstraete, *Shadows of anyons and the entanglement structure of topological phases*, Nature communications **6**(1), 8284 (2015).
- [18] M. Kohmoto, M. den Nijs and L. P. Kadanoff, *Hamiltonian studies of the $d = 2$ ashkin-teller model*, Phys. Rev. B **24**, 5229 (1981), doi:[10.1103/PhysRevB.24.5229](https://doi.org/10.1103/PhysRevB.24.5229).
- [19] H. Saleur, *Correlation functions of the critical ashkin-teller model on a torus*, Journal of statistical physics **50**, 475 (1988).
- [20] M. Caselle, P. Giudice, F. Gliozzi, P. Grinza and S. Lottini, *K-string tensions at finite temperature and integrable models*, Journal of High Energy Physics **2007**(11), 075 (2007), doi:[10.1088/1126-6708/2007/11/075](https://doi.org/10.1088/1126-6708/2007/11/075).
- [21] Y. Aoun, M. Dober and A. Glazman, *Phase diagram of the ashkin-teller model* (2023), [2301.10609](https://arxiv.org/abs/2301.10609).